



Authigenic formation of Ca-Mg carbonates in the shallow alkaline Lake Neusiedl, Austria

Dario Fussmann¹, Avril Jean Elisabeth von Hoyningen-Huene², Andreas Reimer¹, Dominik Schneider², Hana Babková³, Robert Peticzka⁴, Andreas Maier⁴, Gernot Arp¹, Rolf Daniel² and Patrick Meister³

¹Geobiology, Geoscience Centre, Goldschmidtstraße 3, Georg-August-University Göttingen, 37077 Göttingen, Germany

²Genomic and Applied Microbiology Genomics Laboratory, Institute of Microbiology and Genetics, Grisebachstraße 8, Georg-August-University Göttingen, Göttingen, 37077 Germany

³Department of Geodynamics and Sedimentology, University of Vienna, Althanstraße 14, 1090 Vienna, Austria

⁴Department of Geography and Regional Research, University of Vienna, Althanstraße 14, 1090 Vienna, Austria

Correspondence to: Dario Fussmann (dario.fussmann@uni-goettingen.de)

Abstract. Despite advances regarding the microbial and organic-molecular impact on nucleation, the formation of dolomite in sedimentary environments is still incompletely understood. Since 1960, apparent dolomite formation has been reported from mud sediments of the shallow, oligohaline and alkaline Lake Neusiedl, Austria. To trace potential dolomite formation or diagenetic alteration processes in its deposits, lake water samples and sediment cores were analyzed with respect to sediment composition, hydrochemistry and bacterial community composition. Sediments comprise 20 cm of homogenous mud with 60 wt% carbonate, which overlie dark-laminated consolidated mud containing 50 wt% carbonate and plant debris. Hydrochemical measurements reveal a shift from oxic lake water with pH 9.0 to anoxic sediment pore water with pH 7.5. A decrease in SO_4^{2-} with a concomitant increase of $\Sigma\text{H}_2\text{S}$ and NH_4^+ from 0-15 cm core depth, indicates anaerobic heterotrophic decomposition, including sulfate reduction. The bacterial community composition reflects the zonation indicated by the pore water chemistry, with a distinct increase of fermentative taxa below 15 cm core depth.

The water column is highly supersaturated with respect to (disordered) dolomite and calcite, whereas saturation indices of both minerals rapidly approach zero in the sediment. Notably, the relative proportions of different authigenic carbonate phases and their stoichiometric compositions remain constant with increasing core depth. Hence, evidence for Ca-Mg carbonate formation or ripening to dolomite is lacking within the sediment of Lake Neusiedl. As a consequence, precipitation of high-magnesium-calcite (HMC) and very-high-magnesium-calcite (VHMC) does not occur in association with anoxic sediment and sulfate reducing conditions. Instead, analytical data for Lake Neusiedl suggest that authigenic HMC and VHMC precipitate from the supersaturated, well-mixed aerobic water column. This observation supports an alternative concept to dolomite formation in anoxic sediments, comprising Ca-Mg carbonate precipitation in the water column under aerobic and alkaline conditions.



34 1. Introduction

35 Dolomite ($\text{CaMg}[\text{CO}_3]_2$) is the most abundant carbonate mineral in Earth's sedimentary record. It has rarely been
 36 observed forming in recent environments. Instead, most occurrences of large dolomite deposits in the geological
 37 record are the result of pervasive dolomitization of precursor carbonates by fluids with high Mg:Ca ratios and
 38 temperatures during burial (e.g. Machel, 2004). In contrast, the formation of dolomite near the sediment surface,
 39 so-called penecontemporaneous dolomite (Machel 2004 and references therein), or even primary precipitation in
 40 shallow aquatic environments, are often difficult to trace in the rock record and capture in modern environments.
 41 The difficulty in capturing ongoing dolomite formation is due to its peculiar kinetics, which are still incompletely
 42 understood, despite intense laboratory and field experiments. Dolomite does not form in sites where sufficient Ca,
 43 Mg, and carbonate ions are provided, which is generally explained by the high kinetic barrier of dolomite
 44 nucleation and growth (e.g. Lippmann, 1973).

45 Based on the presence of sulfate-reducing bacteria, Vasconcelos et al. (1995) proposed a microbial model, in which
 46 sulfate-reducing bacteria mediate carbonate precipitation, while Brady et al. (1996) consider sulfate ions as
 47 inhibitors for dolomite growth. Further experiments were performed with various different organisms, such as
 48 denitrifiers (Rivadeneira et al., 2000), methanogenic archaea (Roberts et al., 2004) and aerobic halophilic bacteria
 49 (Sánchez-Román et al., 2009). All of these studies showed aggregate formation of carbonate minerals with the
 50 characteristic d_{104} -peak of dolomite under X-ray diffraction, hence, supporting a microbial factor in dolomite
 51 formation. It has been hypothesized that dolomite nucleation is mediated by microbial extracellular polymeric
 52 substances (EPS; Bontognali et al., 2014). However, Gregg et al. (2015) re-analyzed the X-ray diffraction data of
 53 many of the aforementioned microbial experiments, demonstrating that microbial dolomite products lack typical
 54 ordering reflections in XRD spectra and are in fact very high-magnesium-calcite (VHMC or "protodolomite"). In
 55 further studies sulfide (Zhang et al., 2013b) dissolved organic matter (Frisia et al., 2018) or clay minerals (Liu et
 56 al., 2019) were suggested to favor protodolomite nucleation in porefluids. Nevertheless, it is not entirely clear,
 57 which of these factors play a fundamental role in natural environments and how the specific reaction mechanisms
 58 work.

59 While the concept that dolomite forms within sediments mediated by anaerobic microbial processes and their
 60 extracellular polymeric substances, is widely acknowledged, another aspect should be taken into account: The site
 61 of dolomite formation may not always coincide with the location where the mineral is found due to relocation after
 62 precipitation. Several studies describe unlithified dolomite precipitation in warm, arid and hypersaline marine
 63 environments, like coastal sabkhas (Illing et al., 1965; Bontognali et al., 2010; Court et al., 2017), coastal lakes,
 64 such as Lagoa Vermelha in Brazil (Vasconcelos and McKenzie, 1997; van Lith et al., 2002; Sánchez-Román et
 65 al., 2009; Bahniuk et al., 2015) and ephemeral lakes along the Coorong Lagoon in South Australia (von der Borch,
 66 1976; Rosen et al., 1989; Warren, 1990; Wright and Wacey, 2005). Dolomite precipitation is further reported in
 67 endorheic hypersaline lakes, e. g. Lake Qinghai in Tibet (Deng et al., 2010), Lake Acigöl (Turkey; Balci et al.,
 68 2016) and alkaline playa lakes such as Deep Springs Lake in California (Meister et al., 2011).

69 Another Ca-Mg carbonate forming location can be found in Turkey, where McCormack et al. (2018) describe
 70 dolomite in Quaternary sediments from Lake Van, which is suggested to have formed at the sediment-water
 71 interface including varying salinities and low temperatures. These dolomite-bearing deposits have been related to
 72 the onset of a falling paleo lake-level and, hence, changing hydro-chemical conditions. Importantly, McCormack
 73 et al. (2018) locate the formation of dolomite near the sediment-water interface, where it is presumably related to
 74 microbial EPS. However, this area is also exposed to significant fluctuations in pH, temperature, and



75 supersaturation. According to precipitation-experiments conducted by Deelman (1999), dolomite can form due to
 76 such fluctuations in pH and temperature, thereby breaking Ostwald's step rule via undersaturation of other
 77 metastable carbonate phases.

78 Lake Neusiedl is a Ca-Mg carbonate precipitating water body with exceptionally low salinity (1-2 g L⁻¹). It is a
 79 shallow and seasonally evaporative lake in the proximity of Vienna, Austria. Schroll and Wieden (1960) first
 80 reported the occurrence of poorly crystallized dolomite (notable by its broad XRD-reflections) at this locality and
 81 Müller et al. (1972) related its formation to diagenetic alteration of high-magnesium-calcite (HMC). The Mg:Ca
 82 ratios in Lake Neusiedl are unusually high (>7) compared to freshwater lakes, which favor the precipitation of
 83 HMC (Müller et al., 1972). Little is known about the crystallization paths of the Ca-Mg carbonate phases in this
 84 lake, in particular whether they form in the anoxic sediment or oxic water column and if early diagenetic alteration
 85 to dolomite ("ripening") takes place.

86 We revisit the formation of dolomite in Lake Neusiedl by comparing the sediment-geochemical and *in-situ* pore
 87 water data and critically evaluating the location of precipitation. This approach has been used to study dolomite
 88 formation in Lagoa Vermelha (van Lith et al. 2002; Moreira et al., 2004) or in Deep Springs Lake (Meister et al.,
 89 2011). Since 2005, *in-situ* pore water extraction via rhizon samplers has been applied for geoscientific research
 90 questions (Seeberg-Elverfeldt et al., 2005) and several *in situ* pore water studies were conducted using this
 91 technique (e.g. Bontognali, 2010; Birgel et al., 2015; Steiner et al., 2018). A comparable *in-situ* pore water data
 92 set for an oligohaline seasonally evaporative lake, which addresses the question of authigenic Ca-Mg carbonate
 93 precipitation, is absent so far. We further provide bacterial community analyses to address the potential role of
 94 microbes and their metabolisms in a carbonate mineral precipitation or alteration pathway. Hence, our study has
 95 three goals: (i) finding indications for the origin of Ca-Mg carbonate formation, (ii) evaluating the microbiological
 96 and geochemical conditions and their influence on carbonate saturation, and (iii) discussing which factors drive
 97 the formation of Ca-Mg carbonates in Lake Neusiedl.

98 2. Study Area

99 Lake Neusiedl, situated at the Austrian-Hungarian border, is the largest endorheic lake in Western Europe. It is
 100 located in the Little Hungarian Plain, a transition zone between the Eastern Alps and the Pannonian Basin in central
 101 Hungary. The region has been tectonically active since the early Miocene (Horváth, 1993) and is affected by NE-
 102 SW trending normal faults. This early Miocene tectonic activity included the closing of the Central Paratethys Sea
 103 and the formation of Lake Pannon about 11.6 million years ago. This ancient water body was characterized by
 104 highly fluctuating water levels that caused the deposition of local evaporite layers, which influence the salinity of
 105 today's deeper aquifers in the area (Piller et al., 2007; Krachler et al., 2018). The present topography of the Little
 106 Hungarian Plain is the result of ongoing local uplift and subsidence, which commenced in the latest Pliocene
 107 (Zámolyi et al., 2017). Elevated regions are represented by the Rust- and Leitha Hills, which are horst-like
 108 structures located west of Lake Neusiedl. Northward, the water body is separated from the Vienna basin by the
 109 raised Parndorf Plateau, which has a 25-45 m higher surface elevation than the lake area. South- and eastward,
 110 Lake Neusiedl is surrounded by flats, namely the Hansag- and Seewinkel Plain. Despite its proximity to the Alps,
 111 the region surrounding Lake Neusiedl did not have an ice cover during the last glacial maximum. Hence, its
 112 morphology is shaped by periglacial erosion and sedimentation (van Husen, 2004). Throughout the Seewinkel
 113 Plain, Pannonian marine to brackish sediments are largely covered by fluvioglacial gravels. The gravels thin out



westwards and are thus missing beneath parts of Lake Neusiedl, where fine-grained, unlithified lacustrine mud directly overlies compacted Pannonian strata. The absence of a gravel layer has made the former lake area vulnerable to aeolian erosion, favoring the formation of the present day flat trough over tectonic subsidence (Zámolyi et al., 2017).

The surface area of the water body spreads over 315 km² with a maximum depth of 1.8 m. With a salinity of 1-2 g·L⁻¹ and elevated pH values (>8.5), the water chemistry differs significantly from that of freshwater lakes (salinity: < 0.5 g·L⁻¹, pH: 6.5-7.5). Increased amounts of sodium- and bicarbonate ions mainly contribute to the lake's soda-like character (Herzig, 2014). Furthermore, the Mg:Ca ratio is unusually high in comparison to freshwater lakes (Krachler et al., 2012). Permanent surface water inflow is mainly provided by the Rákos and the Wulka streams, which drain a catchment area that is approximately 2.6 times the size of Lake Neusiedl (1,120 km²). Thus, their contribution to the lake's water balance is negligible compared to the significantly higher input from precipitation, providing 80 – 90% of the lake water (Herzig and Dokulil, 2001). As a result of its shallowness and the endorheic drainage system, the lake is very vulnerable to climatic changes, which highly influence the water level, water volume and, hence, the surface area of the lake throughout the year and over the centuries. In the past, Lake Neusiedl was characterized by highly fluctuating water levels and desiccation events (Moser, 1866), the last of which dates back between 1865 and 1870. Since 1910, the lake's water outflow can be regulated by the artificial Hanság- or Einser-Kanal in case of severe flooding events. The canal is located at the lake's southeastern shore (Fig. 1).

More than half (178 km²) of Lake Neusiedl's surface area is covered with reed. Due to its wind exposure and shallowness, the water column of the open water area is well mixed and contains high amounts of suspended particles. The wind sheltering effect of *Phragmites* spears, in contrast, leads to clearer water in the reed belt. Clastic input into the water body is minor and reflects the mineralogical composition of the western neighboring Rust- and Leitha hills, which are characterized by crystalline rocks of the Eastern Alpine basement and Miocene marine carbonates ("Leithakalk", Fig. 1). The deposits forming the present bed of Lake Neusiedl consist of fine-grained mud, which mainly contains typical authigenic carbonate phases such as Mg-calcite and dolomite/VHMC (Löffler, 1979). Those phases can clearly be distinguished from pure calcite, which is considered as allochthonous in the sedimentary environment of Lake Neusiedl (Müller et al., 1972). It is noteworthy, that the mud volume has doubled in the time from 1963 to 1988, leading to an increase of the volumetric mud/water ratio from 36:64 in 1963, to 49:51 in 1988. This mud layer covers the whole lake area and would yield an average thickness of 64 cm, assuming an equal distribution across the lake basin (Bácsatyai, 1997). The soft sediment thickness can increase up to 1 m at the border of the reed belt and open water, where *Phragmites* spears act as sediment traps for current driven, suspended particles (Löffler 1979).

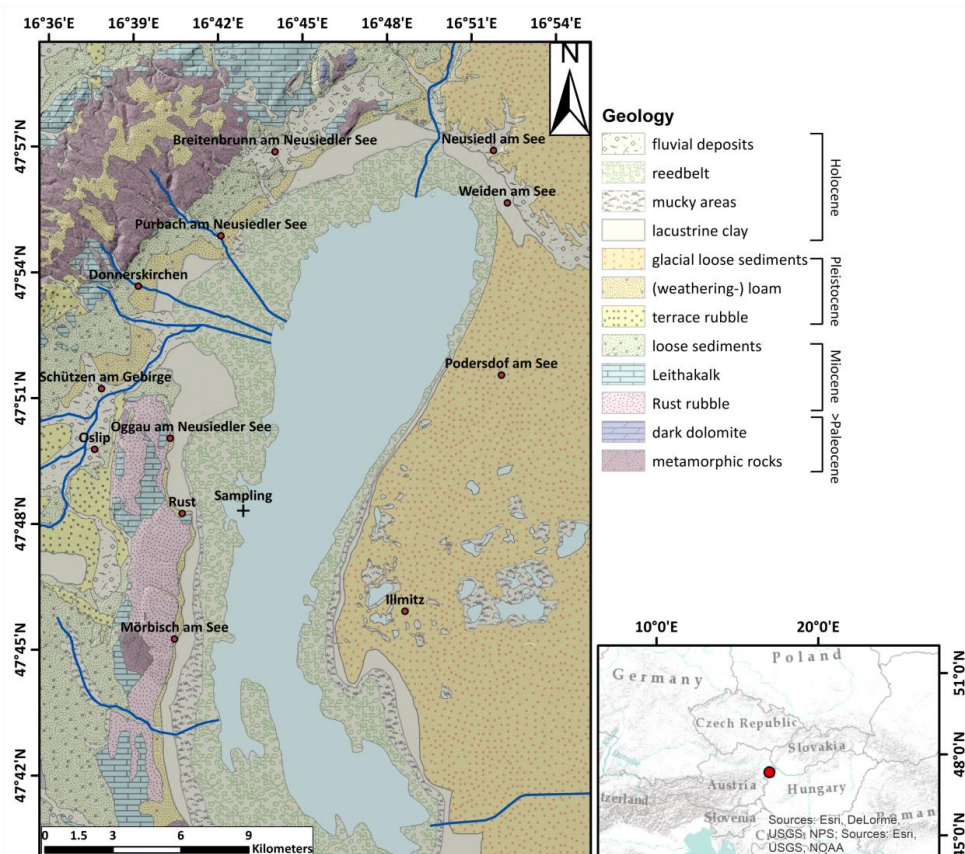


Figure 1: Lake Neusiedl and its surrounding geology, redrawn and simplified after Herrman et al. (1993).

3. Material and Methods

3.1 Sampling and field measurements

The sampling campaign at Lake Neusiedl was performed in August 2017 in the bay of Rust (16°42'33.635"E, 47°48'12.929"N) situated at the lake's central western shore. A pedalo boat was utilized to enable sampling approximately 500 m offshore. Physicochemical parameters of the lake water were measured directly in the field using a WTW Multi 3430 device equipped with a WTW Tetracon 925 conductivity probe, a WTW FDO 925 probe for dissolved O₂, and a WTW Sentix 940 electrode for temperature and pH (Xylem, Rye Brook, NY, USA), calibrated against standard pH-buffers 7.010 and 10.010 (HI6007 and HI6010, Hanna Instruments, Woonsocket, RI, USA; standard deviation ≤ 2%). Lake water was retrieved from a depth of 10 cm with a 500 ml Schott-Duran glass bottle without headspace from which subsamples for anion, nutrient and total alkalinity determination were distributed into 100 mL polyethylene (PE) and 250 mL Schott-Duran glass bottles (Schott, Mainz, Germany), respectively. For cation analysis, a 50 mL aliquot was filtered through membrane filters with a pore size of 0.7 μm (Merck, Darmstadt, Germany) into a PE-bottle and acidified with 100 μl HNO₃ (sub-boiled). Total alkalinity was determined via titration within 3 hours after sampling using a hand-held titration device and 1.6 N H₂SO₄ cartridges (Hach Lange, Düsseldorf, Germany; standard deviation ≤ 1.5%).



Five sediment cores, with the sample codes LN-K01, LN-K02, LN-K03, LN-K04 and LN-K05, were retrieved using PVC-tubes (6.3 cm diameter; Uwitec, Mondsee, Austria) in approximately 30 cm lateral distance. All cores were 30 to 40 cm in length and were used for sediment, pore water and bacterial community profiling. Cores LN-K01 and LN-K02 were subsampled and treated for bacterial community profiling as described in von Hoyningen-Huene et al. (2019) directly after recovery. Cores LN-K03, LN-K04 and LN-K05 were hermetically sealed after recovery and stored upright at temperatures close to their natural environment (22 ± 2 °C). Effects of pressure differences are neglectable in the present case, because the cores were sampled just below the lake floor.

3.2 Petrographic, mineralogical, and geochemical analyses

Two cores, labelled LN-K04 and LN-K05, were used for sediment geochemical and petrographic analyses. Sediment dry density and porosity were calculated from the corresponding sediment weights and volumes. For bulk organic and inorganic carbon content detection, sediment increments of 2.5 cm were subsampled from core LN-K04. They were freeze dried and powdered with a ball mill, before they were measured by a LECO RC612 (Leco, St Joseph, MI, USA) multi-phase carbon and water determination device. For calibration, Leco synthetic carbon (1 and 4.98 carbon%) and Leco calcium carbonate (12 carbon%) standards were used. The same increments were utilized for CNS elemental detection, which was operated with a Euro EA 3000 Elemental Analyzer (Hekatech, Wegberg, Germany). 2.5-Bis (5-tert-benzoxazol-2-yl) thiophene BBOT and atropine sulfate monohydrate (IVA Analysetechnik, Meerbusch, Germany) were provided as reference material. Analytical accuracy of all analyses was better than 3.3%.

XRD-analyses were conducted with identical increments at the Department of Geodynamics and Sedimentology in Vienna by a PANalytical (Almelo, Netherlands) Xpert Pro device ($\text{CuK}\alpha$ radiation, 2θ refraction range of $2-70^\circ$, and a step size of 0.01°). Semi-quantitative phase composition analysis was performed with Rietveld refinement of peak intensities by using MAUD (version 2.8; Lutterotti et al., 2007). To ensure a better reproducibility of the semi-quantitative XRD-analysis, Rietveld refined results were compared and correlated with carbon data retrieved from the aforementioned LECO RC612 device.

In core LN-K05, sediment increments of 5 cm were subsampled for thin sectioning and light microscopic observations. To ensure a continuous section, rectangular steel meshes, 5 cm in length, were placed along the sediment column. These steel meshes, filled with soft sediment, were then embedded in LR White resin (London Resin Company, Reading, United Kingdom), after a dehydration procedure with ethanol. During dehydration, the sediments were treated with Sytox Green nucleic acid stain (Invitrogen, Carlsbad, CA, USA) to stain eukaryotic cell nuclei and prokaryotic cells for fluorescence microscopy. Samples were cured for 24 hours at 60°C before thin section preparation. The thin sections were ground down to a thickness of 40 to 50 μm and then capped with a glass cover. Petrographic observations were conducted with a petrographic and a laser-scanning microscope (Zeiss, Oberkochen, Germany, lsm excitation: 543 nm, 488 nm, 633 nm, laser unit: Argon/2, HeNe543, HeNe633). For scanning electron microscopy, non-capped unpolished thin section fragments and freeze-dried loose sediment from cores LN-K05 and LN-K04 were placed on 12.5 mm plano carriers and sputtered with a platinum-palladium mixture. Field emission scanning electron microscopy was conducted with a Gemini Leo 1530 device (Zeiss, Oberkochen, Germany) with a coupled INCA x-act (Oxford Instruments, Abingdon, United Kingdom) EDX detector.



201 3.3 Pore water analysis

202 Redox potential and pH gradients were directly measured in the sediment of core LN-K03 one week after sampling
 203 with a portable WTW 340i pH meter, equipped with an Inlab Solids Pro pH-electrode (Mettler Toledo, Columbus,
 204 OH, USA) and a Pt 5900 A redox electrode (SI Analytics, Mainz, Germany) through boreholes (standard deviation
 205 $\leq 2\%$). Pore water was extracted from the core, using 5 cm CSS Rhizon samplers (Rhizosphere, Wageningen,
 206 Netherlands). Immediately after extraction, aliquots were fixed with Zn-acetate for determination of total sulfide
 207 ($\Sigma\text{H}_2\text{S}$). Pore water alkalinity was determined using a modified Hach titration method with self-prepared 0.01 N
 208 HCl cartridges as titrant. Major cation (Ca^{2+} , Mg^{2+} , Na^+ , K^+ and Li^+) and anion (Cl^- , F^- , Br^- , SO_4^{2-} and NO_3^-)
 209 concentrations of lake and pore water samples (including supernatants in the cores) were analyzed by ion
 210 chromatography with non-suppressed and suppressed conductivity detection, respectively (Metrohm 820 IC /
 211 Metrosep C3-250 analytical column, Metrohm 883 Basic IC/ Metrohm ASupp5-250 analytical column, Metrohm,
 212 Herisau, Switzerland; standard deviation $\leq 2\%$). Inductively coupled plasma mass spectrometry (ICP-MS; ICAP-
 213 Q, Thermo Fisher, Waltham, MA, USA) was used to determine Sr, Ba, Fe, Mn, Rb and B, as control for the cation
 214 determination by ion chromatography (standard deviation $\leq 3\%$).

215 Concentrations of NH_4^+ , NO_2^- , PO_4^{3-} , $\Sigma\text{H}_2\text{S}$ and dissolved silica ($\text{SiO}_{2(\text{aq})}$) were measured by photometric methods
 216 according to Grasshoff et al. (2009), using a SI Analytics Uviline 9400 spectrophotometer. In addition, methane
 217 and dissolved inorganic carbon (DIC) amounts were retrieved from a different core, sampled at the same locality
 218 in August 2017. Methane concentrations were determined from 5 cm³ sediment samples stored upside down in
 219 gas-tight glass bottles containing 5 mL NaOH (5% w/v). Aliquots of 5 ml headspace methane were transferred to
 220 evacuated 10 ml vials. The aliquots were analyzed with an automated headspace gas chromatograph (GC Agilent
 221 7697A coupled to an Agilent 7890B auto sampler) at the University of Vienna. Methane concentrations were
 222 quantified at a runtime of 1.798 min by a flame ionization detector and a methanizer. For linear calibration, a
 223 standard series with the concentrations 1001 ppb, 3013 ppb and 10003 ppb was used. DIC concentrations were
 224 retrieved by using a Shimadzu TOC-LCPH (Shimadzu, Kyoto, Japan) analyzer with an ASI-L autosampler and a
 225 reaction vessel containing a reaction solution of phosphoric acid (H_3PO_4 , 25%). The DIC was measured by
 226 conversion to carbon dioxide, which was detected by a NDIR detector.

227 All measured values were processed with the PHREEQC software package (version 3; Parkhurst and Appelo,
 228 2013). The implemented phreeqc.dat and wateqf4.dat databases were used in order to calculate ion activities and
 229 pCO_2 (partial pressure of CO_2) of the water samples and mineral saturation states. The saturation indices of mineral
 230 phases are given as $\text{SI} = \log (\text{IAP}/K_{\text{SO}})$.

231 3.4 Bacterial 16S rRNA gene community profiling

232 Two sediment cores labelled LN-K01 and LN-K02 were sampled for bacterial 16S rRNA gene-based community
 233 profiling. Each core was sampled in triplicate at every 2.5-5 cm of depth and the surface water filtered through a
 234 2.7 (Merck, Darmstadt, Germany) and 0.2 μm (Sartorius, Göttingen, Germany) filter sandwich. RNAprotect
 235 Bacteria Reagent (Qiagen, Hilden, Germany) was immediately added to all samples, in order to preserve the
 236 nucleic acids. Before storage at -80°C , the samples were centrifuged for 15 min at $3.220 \times g$ and the RNAprotect
 237 Bacteria Reagent was decanted.

238 DNA was extracted and 16S rRNA genes were amplified and sequenced as described in detail by von Hoyningen-
 239 Huene et al. (2019). Briefly, DNA was extracted from 250 mg of each homogenized sediment sample or one third
 240 of each filter with the MoBio PowerSoil DNA isolation kit (MoBio, Carlsbad, CA, USA) according to



241 manufacturer's instructions with an adjusted cell disruption step. Bacterial 16S rRNA genes were amplified in
 242 triplicate by PCR with the forward primer D-Bact-0341-b-S-17 and the reverse primer S-D-Bact-0785-a-A-21
 243 (Klindworth et al., 2013) targeting the V3-V4 hypervariable regions. Primers included adapters for sequencing on
 244 an Illumina MiSeq platform. PCR triplicates were pooled equimolar and purified with MagSi-NGS^{Prep} magnetic
 245 beads (Steinbrenner, Wiesenbach, Germany) as recommended by the manufacturer and eluted in 30 µl elution
 246 buffer EB (Qiagen, Hilden, Germany).
 247 PCR products were sequenced with the v3 Reagent kit on an Illumina MiSeq platform (San Diego, CA, USA) as
 248 described by Schneider et al. (2017). Sequencing yielded a total of 6,044,032 paired-end reads, which were quality-
 249 filtered (fastp, version 0.19.4; Chen et al., 2018), merged (PEAR, version 0.9.11; Zhang et al., 2013a) and
 250 processed. This comprised primer clipping (cutadapt, version 1.18; Martin, 2011), size-filtering, dereplication,
 251 denoising and chimera removal (VSEARCH, v2.9.1; Rognes et al., 2016). Taxonomy was assigned to the resulting
 252 amplicon sequence variants (ASVs; Callahan et al., 2017) via BLAST 2.7.1+ against the SILVA SSU 132 NR
 253 (Quast et al., 2012). After taxonomic assignment, 2,263,813 merged reads remained in the dataset. The resulting
 254 ASV abundance table was used for the visualization of community gradients along the cores (von Hoyningen-
 255 Huene et al., 2019). Data were analyzed using R (version 3.5.2; R Core Team, 2018) and RStudio (version 1.1.463;
 256 RStudio; R Team, 2016) using the base packages. Extrinsic domains, archaea and eukaryotes were removed from
 257 the ASV table for analysis. All ASVs with lower identity than 95% to database entries were assigned as
 258 unclassified. Replicates for each depth were merged, transformed into relative abundances and all ASVs with an
 259 abundance > 0.5% were summarized by their phylogenetic orders. Putative functions of all orders were assigned
 260 according to literature on cultured bacterial taxa and the closest cultured relatives of the ASVs present in our
 261 samples. For uncultured taxa, functions were inferred from literature on genomic and metagenomic sequencing
 262 data (Suppl. Material Tab. S6). The resulting table with relative abundances and functional assignments was used
 263 to generate bar charts in SigmaPlot (version 11; Systat Software, 2008).

264 **4. Results**

265 **4.1 Sediment petrography and mineralogy**

266 The cored sediment can be divided into three different lithological units. Unit I, in the first 15 cm below surface
 267 (b.s.), is characterized by homogenous, light to medium grey mud with very high water content and porosity (>65
 268 weight%, 0.67). The mud consists of very fine-grained carbonate and siliciclastics, largely in the clay and silt size
 269 fraction. In the thin sections of embedded mud samples, carbonates make up most of the fine-grained matrix (Fig.
 270 2A and B). Remnants of diatoms and ostracods occur with random orientation. Detrital grains up to fine sand
 271 fraction, consisting of quartz, feldspar, mica, chlorite and carbonates make up as much as 20% of the sediment.
 272 The latter are distinguishable from authigenic carbonate phases by their bigger (up to mm measuring) size and
 273 fractured shape. The $C_{org}:N_{tot}$ ratio scatters around 10 (Fig. 3) and plant detritus is evident in thin sections as
 274 opaque, up to several hundred µm in size, often elongated and randomly orientated particles (Fig. 2A and B).
 275 These can be identified in the laser scan images, due to their chlorophyll related bright fluorescence (Fig. 4A and
 276 B).
 277 Unit II is located between 15 and 22 cm b.s. and appears as slightly darker, grey-colored mud without
 278 macrostructures. The microcrystalline matrix appearance is similar to Unit I, however, phytoclasts and detrital
 279 mineral grains are more abundant and up to mm in size, whereas the amount of bioclasts remains the same.



280 Noticeably, detrital carbonate minerals and quartz grains occur layer-like or in defined lenses (Fig. 2C and D). The
 281 component to matrix ratio slightly increases up to 25:75% and cubic, small (up to 10 μm), opaque minerals often
 282 occur intercalated with plant detritus. The $C_{\text{org}}:N_{\text{tot}}$ ratio also changes from 10 at 15 cm to 12 at 22 cm b.s..
 283 Unit III, occurs from 22 to 40 cm b.s.. It is distinctly darker than the units above and shows a significant decrease
 284 in water content and porosity to <50 weight% and <0.6, respectively. This decrease in porosity is also recognizable
 285 by a more cohesive sediment texture. Lamination is visible at the core's outer surface, but not in the cut section, in
 286 which plant detritus noticeably increases. Thin sections of this unit illustrate a rather compacted matrix, a
 287 horizontal orientation of elongated phytoclasts and a layered structure with detrital mineral grains (Fig. 2E and F),
 288 further supported by the laser scan image (Fig. 4C). Ostracod or diatom fragments still occur but are less abundant
 289 than in the units above. The particle to matrix ratio increases up to 35:65% and the $C_{\text{org}}:N_{\text{tot}}$ ratio steadily increases
 290 from 12 to 14 through Unit III.

291 In SEM images, the matrix appears as microcrystalline aggregate of several nanometer-sized clotted crumbs (Fig.
 292 5). Locally, small, up to 1 μm in scale, irregularly shaped rhombohedral crystals are observable. With EDX
 293 measurements, these tiny crystals were identified as Ca-Mg carbonate phases.

294 According to the XRD spectra, the bulk sediment mainly consists of carbonates and quartz with minor
 295 contributions of feldspar, clay, and mica (Fig. 6). The d_{104} peak shift provides a suitable approach to estimate the
 296 Mg:Ca ratio in magnesium calcite and dolomite (Lumsden, 1979). Based on the d_{104} peak positions, three carbonate
 297 phases with different MgCO_3 -content are present: A calcite phase with minor amounts of MgCO_3 , a high-
 298 magnesium-calcite phase (HMC) with circa 18 mole% MgCO_3 and a very-high-magnesium-calcite phase (VHMC,
 299 Fig. 6). The latter shows a 104 peak, shifted from $31^\circ 2\theta$ in ordered dolomite to ca. $30.8^\circ 2\theta$, indicating a MgCO_3
 300 content of approx. 45 mole%. Estimated relative mineral abundances vary between the three units (Fig. 7): In Unit
 301 I the amount of authigenic carbonate minerals remains relatively constant at 55 weight%, whereas in Unit II a
 302 steep/large increase of detrital mineral phases (feldspar, quartz, calcite, mica) can be found. In Unit III the amount
 303 of Ca-Mg carbonate phases decreases and scatters around 40 weight%. Mica slightly increase with depth below
 304 23 cm. Nevertheless, the authigenic HMC to VHMC ratio does not change significantly throughout the section.
 305 Notably, all authigenic Ca-Mg carbonate phases do not show any down-core trend in stoichiometry. The
 306 $\text{Mg}/(\text{Ca}+\text{Mg})$ ratios of distinct solid phases remain largely constant with depth (Fig. 8).

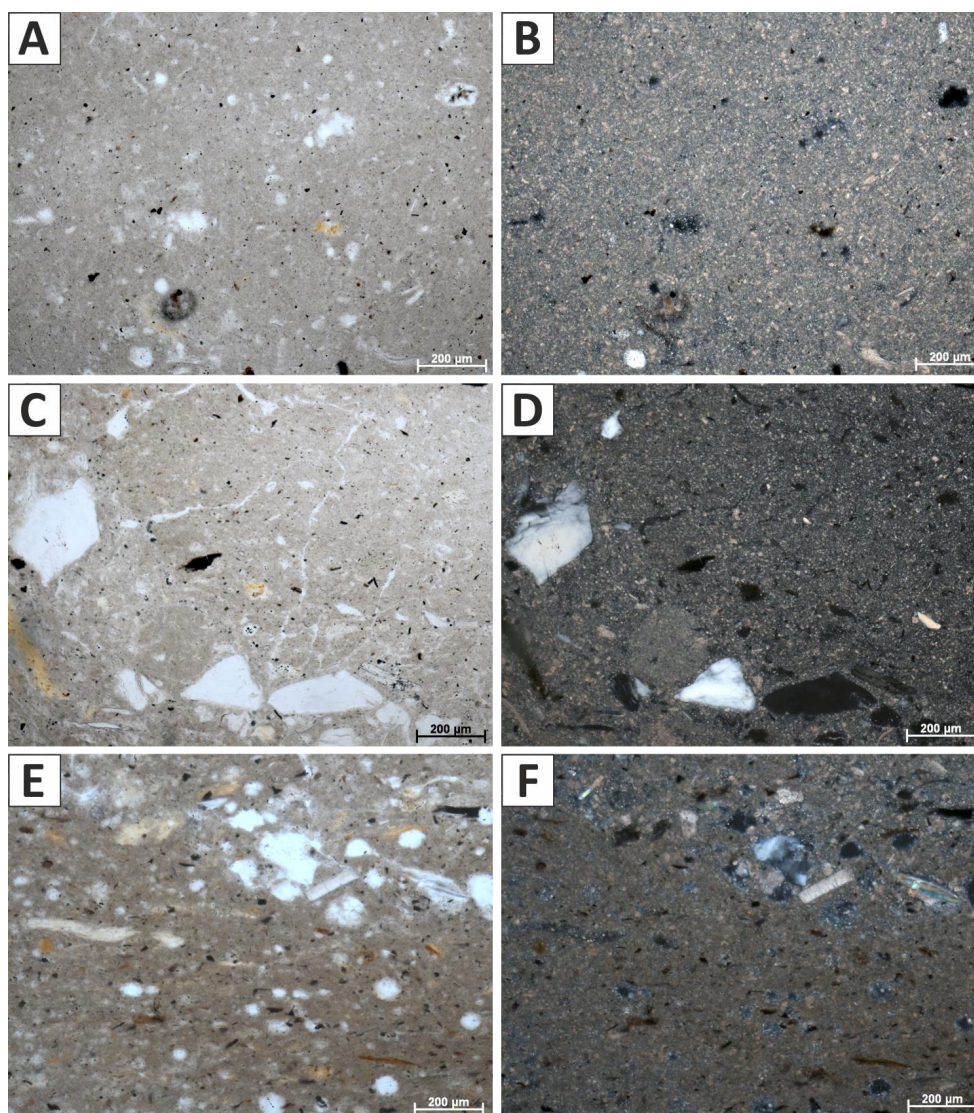


Figure 2: (A) Microfabric of Unit I at 5 cm depth in transmitted light. Note the randomly oriented, opaque and brownish plant particles. The microcrystalline matrix is more apparent in polarized light (B). (C) Microfabric overview of Unit II at 17 cm depth. Large, up to fine sand-scale detrital feldspar grains occur in layers. (D) Same image section in polarized light. (E) Microfabric of Unit III at 28 cm, illustrating the rather compacted shape of the matrix and the elongated appearance of plant detritus. The layering is evident by the occurrence of larger detrital grains in the upper image part. (F) Same section in polarized light.

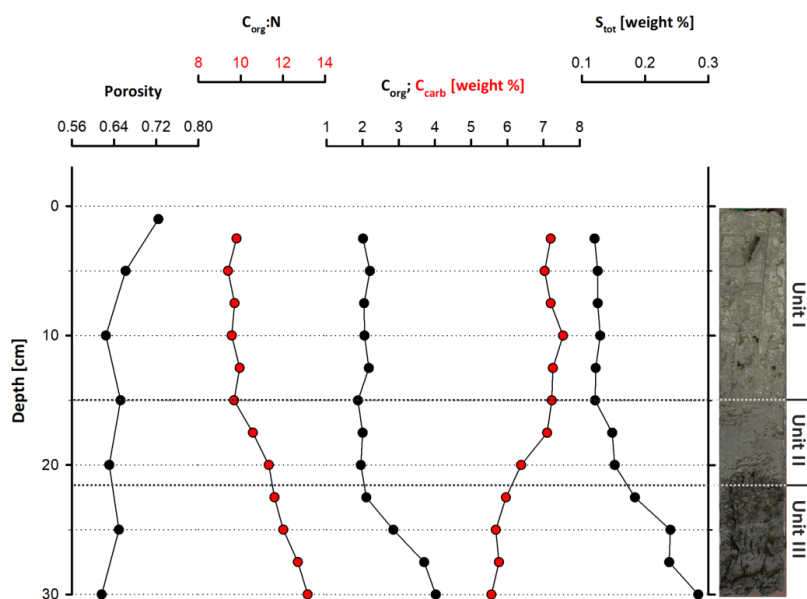


Figure 3: Geochemical parameters through Core LN-K04, showing an increasing amount of organic carbon, total sulfur and a decreasing porosity with depth.

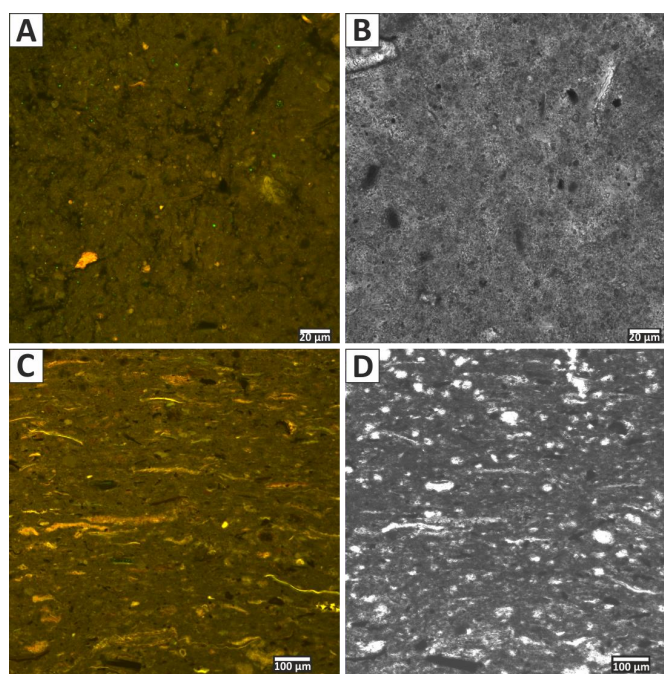
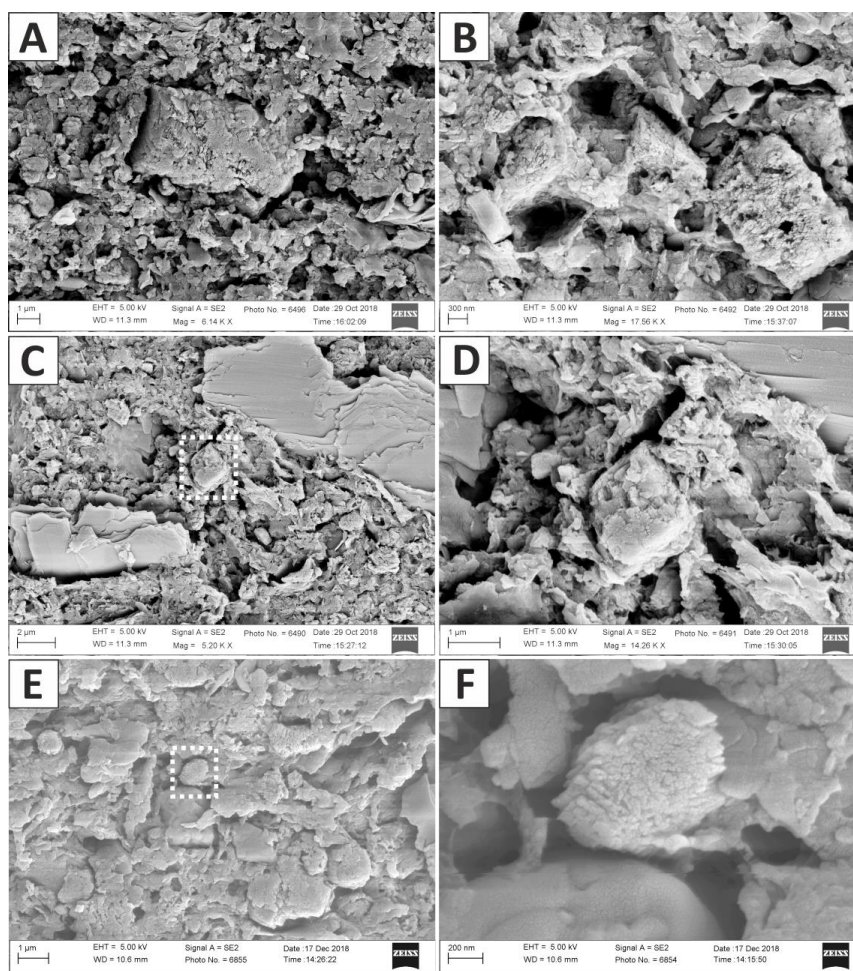


Figure 4: (A) Laser scanning micrograph (excitation 365 nm/emission 397-700 nm) of Unit I microfabric at 2 cm depth. The small, and randomly orientated plant particles show bright fluorescence due to their chlorophyll content. (B) Same section in transmitted light. (C) Fluorescent texture of Unit III (at 28 cm depth) is visible. The higher amount of plant detritus, particle layering and a compacted matrix are notable. Voids are resin embedding artefacts. (D) Same section as in (C) under transmitted light.



324

325 **Figure 5:** SEM images of Core LN-K 05, showing the crystal morphology of Ca-Mg phases with increasing depth. (A)
 326 HMC/VHMC/dolomite crystal in 9 cm depth. (B) Aggregate of 3 HMC/VHMC/dolomite crystals in 17 cm depth. (C)
 327 Matrix overview containing microcrystalline crumbs, layered mica crystals and a HMC/VHMC rhombohedron
 328 (indicated by dashed rectangle) at 17 cm depth. (D) Detail of rhombohedron visible in C. (E) Matrix overview in 27 cm
 329 depth. HMC/VHMC carbonate crystals appear rather xenomorphic (indicated by dashed rectangle). (F) Close up of
 330 HMC/VHMC crystal accentuated in (E).

331

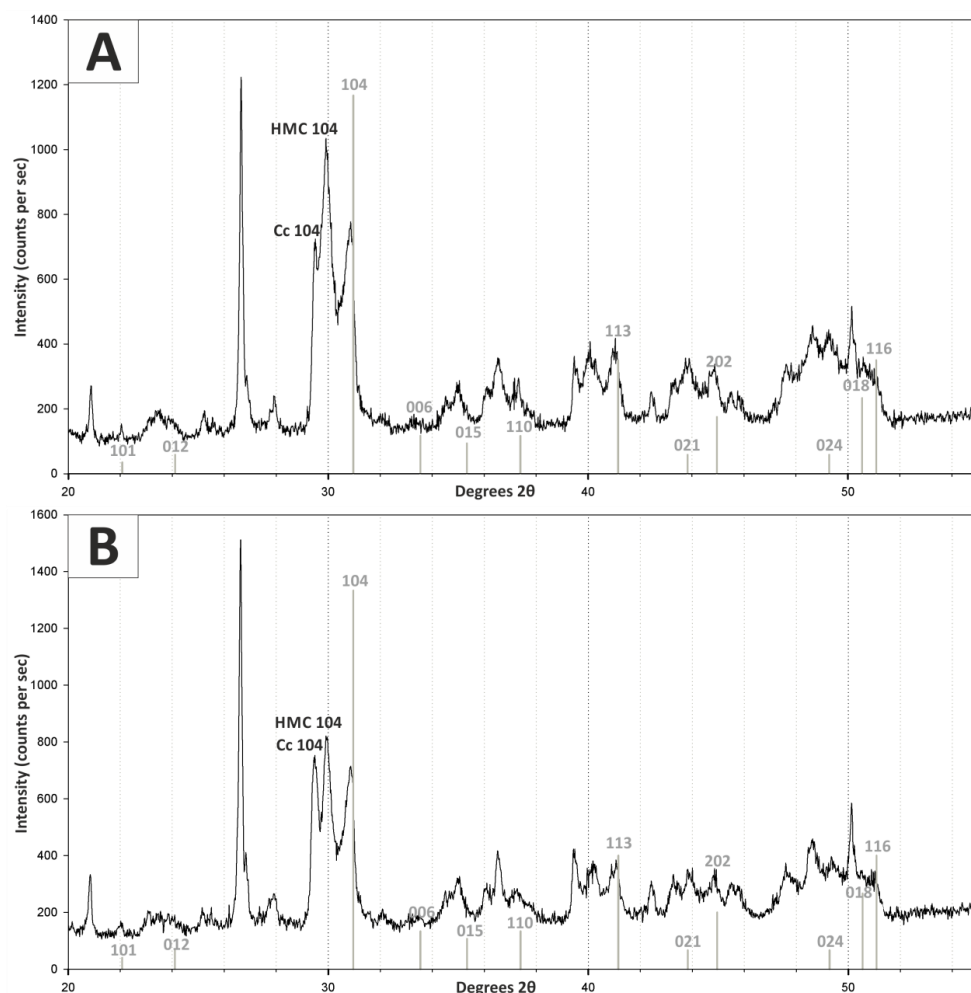
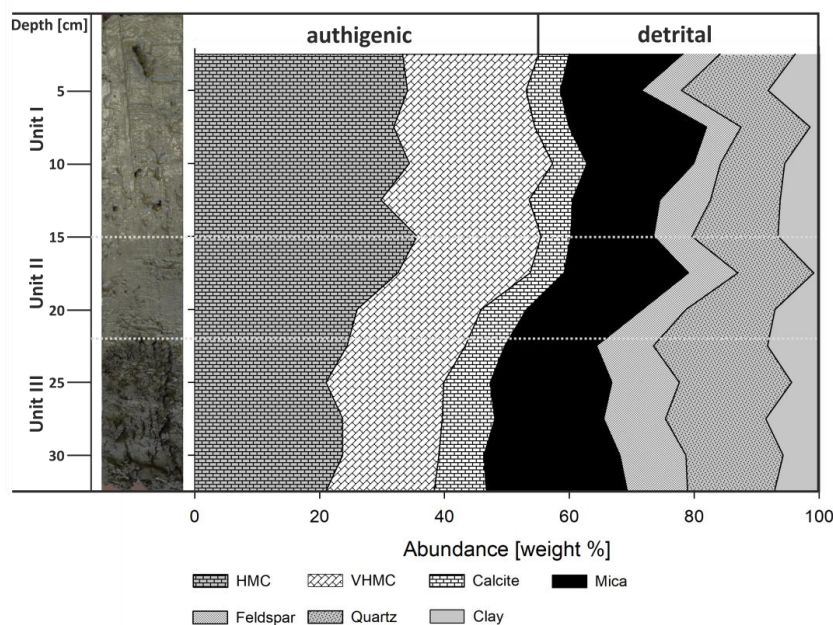
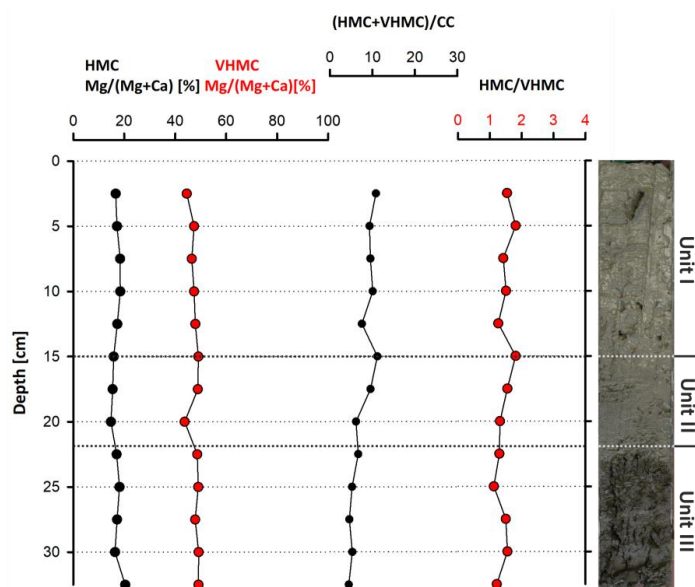


Figure 6: X-ray diffractograms of bulk Lake Neusiedl sediment (A) from 2 cm and (B) from 27.5 cm depth. Positions of dolomite ordering peaks are marked in grey. Position of major calcite (Cc 104) and high-magnesium-calcite (HMC 104) peaks are also indicated. Note that no ordered dolomite can be identified in the investigated Lake Neusiedl samples.



337

338 **Figure 7: Core LN-K04 with the defined units I-III (left) and mineral quantities estimated from main peak heights**
 339 **(right; HMC: high-magnesium calcite, VHMC: very-high-magnesium calcite). The changes of mineral abundances**
 340 **coincide with unit boundaries.**



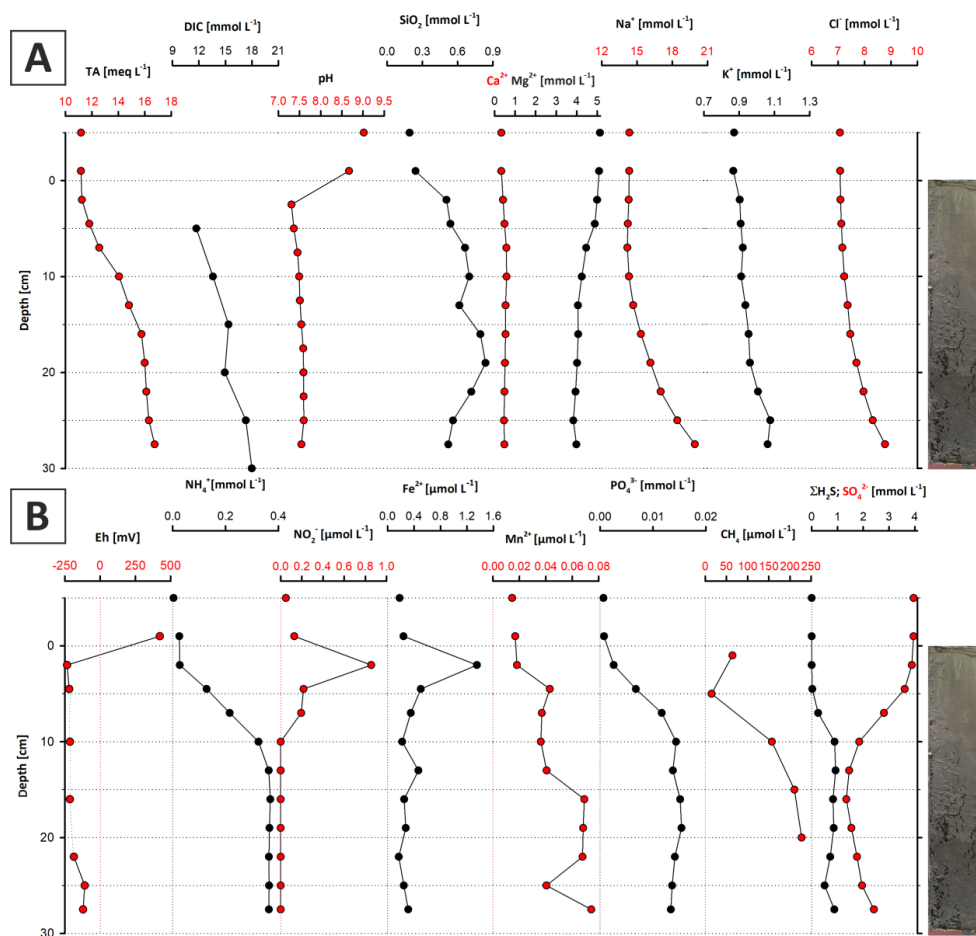
341

342 **Figure 8: Stoichiometric compositions of authigenic carbonate phases (HMC and VHMC), their abundance ratio, and**
 343 **their relation to detrital calcite.**



344 4.2 Pore water chemistry

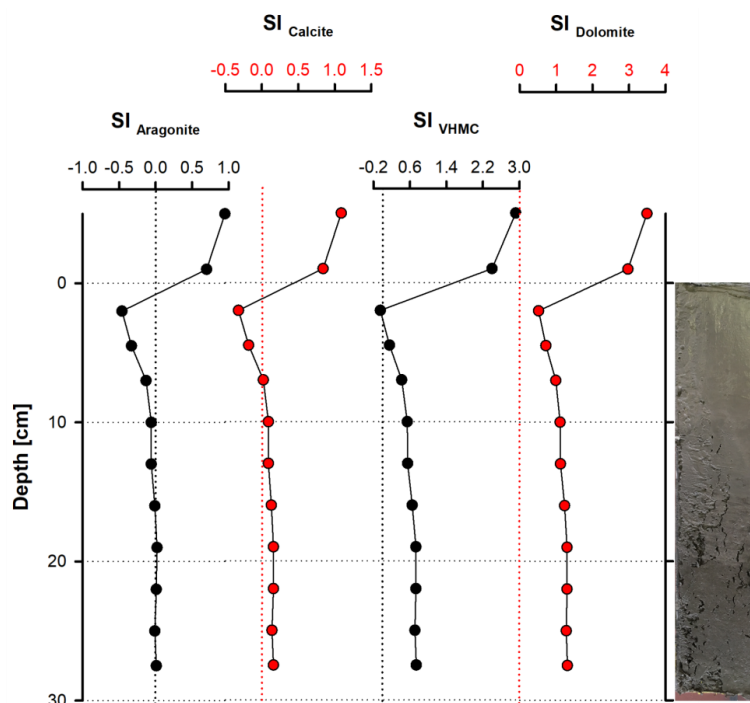
345 The water chemistry of Lake Neusiedl is characterized by high pH values (9.02) and moderate salinity (1.8‰).
 346 Sodium (Na^+) and magnesium (Mg^{2+}) are the major cations with concentrations of 14.3 and 5.1 $\text{mmol}\cdot\text{L}^{-1}$,
 347 respectively. Calcium (Ca^{2+}) concentration is considerably lower at 0.3 $\text{mmol}\cdot\text{L}^{-1}$. Total alkalinity (TA) measures
 348 11.2 $\text{meq}\cdot\text{L}^{-1}$ whereas other major anions like chloride (Cl^-) and sulfate (SO_4^{2-}) hold a concentration of 7 and 4
 349 $\text{mmol}\cdot\text{L}^{-1}$, respectively. Nutrient (NH_4^+ , NO_2^- , PO_4^{3-} , $\Sigma\text{H}_2\text{S}$, $\text{SiO}_{2(\text{aq})}$) concentrations lie below 0.004 $\text{mmol}\cdot\text{L}^{-1}$.
 350 The pore water chemistry strongly differs between the sediment and the water column. The pH drops significantly
 351 at the water-sediment interface to a value around 7.5, which stays constant throughout the sediment core (Fig. 9A).
 352 The entire section is anoxic with a redox potential of -234 mV at the top, which increases to -121 mV at the bottom
 353 (Fig. 9B). Na^+ and Cl^- contents continuously increase with depth from 14 to 20 and from 7 to 8.8 $\text{mmol}\cdot\text{L}^{-1}$,
 354 respectively (Fig. 9A). Mg^{2+} and Ca^{2+} show a different pattern: From 5 to 10 cm depth, the Mg^{2+} content decreases
 355 from 5 to 4 $\text{mmol}\cdot\text{L}^{-1}$, whereas the Ca^{2+} content increases from 0.5 to 0.6 $\text{mmol}\cdot\text{L}^{-1}$ in the same increment. From
 356 10 cm downwards, the Mg^{2+} content scatters around 4 $\text{mmol}\cdot\text{L}^{-1}$ and the Ca^{2+} content decreases from 0.6 to below
 357 0.5 $\text{mmol}\cdot\text{L}^{-1}$ (Fig. 9A). Dissolved SO_4^{2-} and hydrogen sulfide ($\Sigma\text{H}_2\text{S}$) also show a noticeable trend: The $\Sigma\text{H}_2\text{S}$
 358 content is close to zero in the top 5 cm of the sediment column, rapidly increases to 1 $\text{mmol}\cdot\text{L}^{-1}$ between 5 and 10
 359 cm b.s. and remains constant to the bottom of the section. SO_4^{2-} follows an opposite trend. Its concentration
 360 decreases from 4 to 1 $\text{mmol}\cdot\text{L}^{-1}$ in the upper 10 cm b.s. and remains constant at 1 $\text{mmol}\cdot\text{L}^{-1}$ towards the section
 361 bottom. Total alkalinity also increases towards the lower part of the section, from 11.2 to 16.8 $\text{meq}\cdot\text{L}^{-1}$, with an
 362 increase between 5 and 15 cm depth.
 363 NO_2^- is present in the upper 10 cm of the core and reaches its highest value (0.9 $\mu\text{mol}\cdot\text{L}^{-1}$) at 2 cm b.s., while its
 364 concentration decreases to zero below 10 cm b.s.. Dissolved iron (Fe^{2+}) has a similar trend in the upper 10 cm b.s.,
 365 reaching its highest concentration at a depth of 2 cm (1.4 $\mu\text{mol}\cdot\text{L}^{-1}$). Below 10 cm core depth, iron concentrations
 366 lie below 0.3 $\mu\text{mol}\cdot\text{L}^{-1}$, with the exception of an outlier value of 0.5 $\mu\text{mol}\cdot\text{L}^{-1}$ at 13 cm b.s.. Concentrations of
 367 ammonia (NH_4^+) and phosphate (PO_4^{2-}) increase with depth. In the uppermost part of the sediment column, they
 368 are close to zero and increase to 0.37 and 0.02 $\text{mmol}\cdot\text{L}^{-1}$ at 13 cm. These values remain constant to the bottom of
 369 the core. Dissolved silica shows a curved profile with 0.3 $\text{mmol}\cdot\text{L}^{-1}$ at the top, reaching a maximum at 15 cm depth
 370 with 0.8 $\text{mmol}\cdot\text{L}^{-1}$ and declines to concentrations around 0.5 $\text{mmol}\cdot\text{L}^{-1}$. Methane (CH_4) concentration also shows
 371 a curved trend, reaching its highest value of 227 $\mu\text{mol}\cdot\text{L}^{-1}$ at a depth of 20 cm and concentrations between 14 and
 372 64 $\mu\text{mol}\cdot\text{L}^{-1}$ close to the sediment surface (5 and 1 cm, respectively). Dissolved inorganic carbon (DIC) increases
 373 from 11.71 $\text{mmol}\cdot\text{L}^{-1}$ at the top to 18.01 $\text{mmol}\cdot\text{L}^{-1}$ at 30 cm depth. Only in the 15 to 20 cm increment, the amount
 374 of DIC slightly decreases from 15.37 to 14.94 $\text{mmol}\cdot\text{L}^{-1}$.
 375 According to PHREEQC calculations, the water column at the sampling site (Bay of Rust) is supersaturated with
 376 respect to aragonite (SI = 0.92), calcite (SI = 1.07), VHMC (SI = 2.92; protodolomite) and dolomite (SI = 3.46;
 377 Fig. 10). Sediment pore water is close to equilibrium throughout the whole section with respect to aragonite,
 378 whereas calcite is in equilibrium to slightly supersaturated between 10 and 27.5 cm depth. VHMC (dolomite d)
 379 reaches equilibrium between 2.5 and 5 cm, while dolomite is supersaturated in the entire section. It should be noted
 380 that all saturation graphs reveal parallel trends, with their highest saturation at 17.5 cm and their lowest at 2.5 cm
 381 depth.



382

383 **Figure 9: Major ion- (A) and metabolite concentrations (B) in the pore water of core LN-K03. Note that the sample**
 384 **slightly above 0 cm depth represents the supernatant water, and the top data points represent the water column (see**
 385 **text for explanations).**

386



387

388 **Figure 10: Saturation indices (SI) of selected carbonate mineral phases. Noteworthy, all phases are clearly**
 389 **supersaturated in the water column but close to saturation throughout most of the sediment column (except for the**
 390 **uppermost 10 cm).**

391 4.3 Bacterial community composition

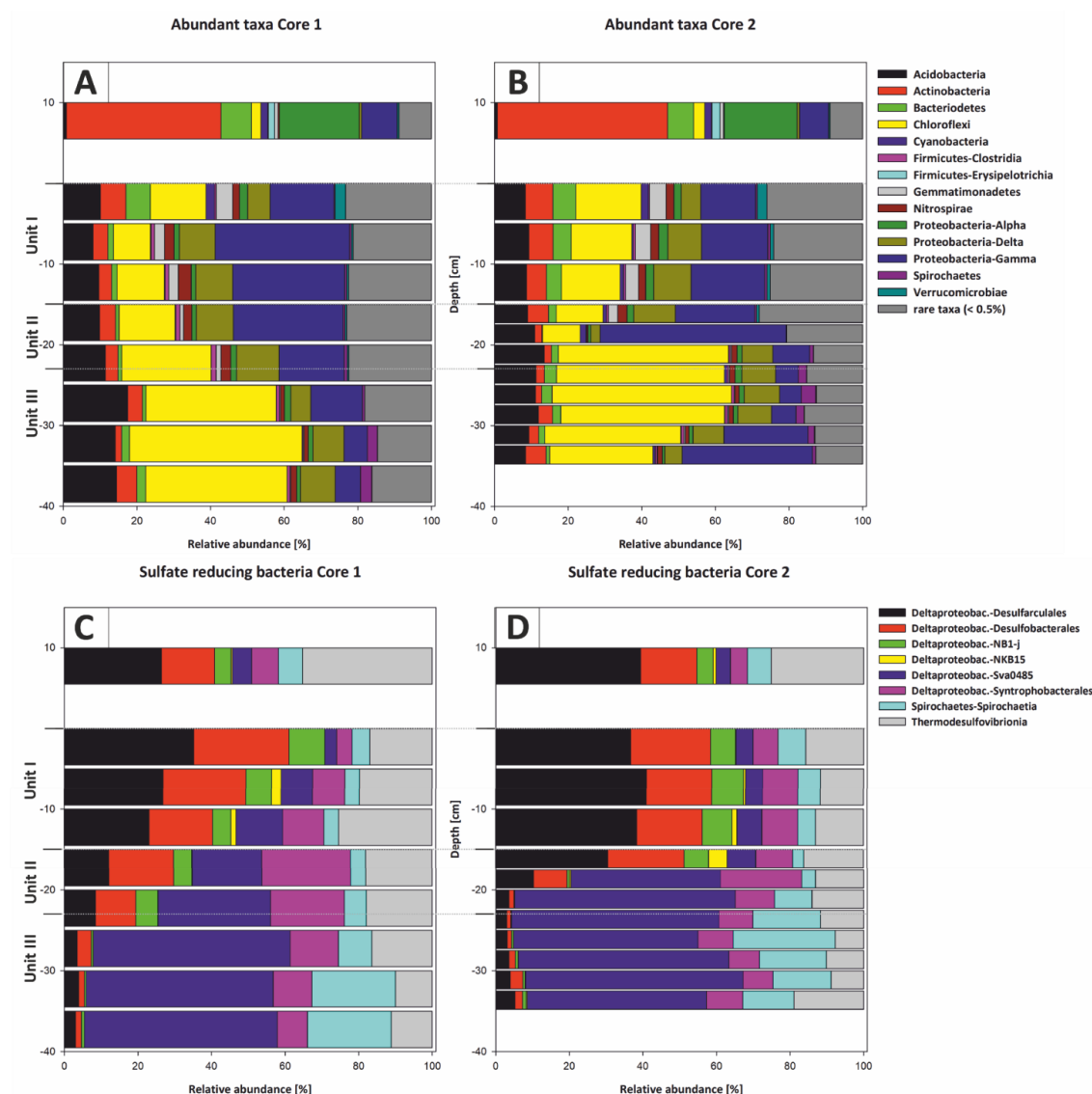
392 Bacterial 16S rRNA gene analysis revealed the presence of a diverse bacterial community with 1,226 amplicon
 393 sequence variants (ASVs) clustered at 100% sequence identity within the water column, 2,085 to 2,467 ASVs in
 394 the top 20 cm of the sediment core and 1,417 to 1,581 ASVs in the deeper sediment (20 - 35 cm core depth). The
 395 different bacterial taxa were grouped by known metabolic properties of characterized relatives, listed in Whitman
 396 (2015) and additional literature (see supplementary data). The distribution of the most abundant bacterial taxa
 397 differs between the water column and the sediment (Fig. 11A and B).

398 The water column is dominated by aerobic heterotrophs, mainly *Alphaproteobacteria* and *Actinobacteria*, which
 399 are only of minor abundance in the sediment. Among the *Alphaproteobacteria*, the SAR 11 clade capable of
 400 oxidizing C1-compounds (Sun et al. 2011), is predominant. The nitrogen-fixing *Frankiales* are the most abundant
 401 representatives of the *Actinobacteria*. Furthermore, coccoid *Cyanobacteria* (*Synechococcales*) and *Bacteroidetes*
 402 are present in high relative abundances in the water column.

403 Within sediment Unit I (0-15 cm b. s.), the bacterial community composition changes to mainly anaerobic and
 404 facultatively anaerobic taxa. Only the uppermost 5 cm show increased relative abundances of *Cyanobacteria*
 405 (*Synechococcales*) and *Bacteroidetes* (aerobes and facultative anaerobes; Alderkamp et al., 2006, Flombaum et
 406 al., 2013), as well as *Verrucomicrobia* (mostly aerobic and facultative anaerobic heterotrophs, He et al. 2017),
 407 which include nitrogen-fixing members (Chiang et al. 2018). Besides these groups, *Gammaproteobacteria*,



408 *Acidobacteria*, *Chloroflexi*, as well as sulfate-reducing *Deltaproteobacteria* are abundant. The latter mainly consist
409 of *Desulfobacteraceae* and *Desulfarculales* (Fig. 11C and D).
410 In sediment Unit II (15-22 cm b. s.), the relative proportions of these groups show a transition between sediment
411 unit I and III. While *Gammaproteobacteria*, *Acidobacteria* and *Deltaproteobacteria* are still abundant, the relative
412 abundance of *Chloroflexi* increases strongly from 24.29 to 35.43%. Within the SRB, *Desulfobacteraceae* and
413 *Desulfarculales* are successively replaced by *Deltaproteobacteria* of the Sva0485 clade. The *Syntrophobacterales*
414 show their maximum relative abundance within sediment unit II.
415 In sediment unit III (22-40 cm b. s.), the abundance of *Chloroflexi* further increases to form the dominant bacterial
416 phylum. The phylum consists of *Dehalococcoidia* and *Anaerolineae*. Other abundant groups in this unit are
417 *Acidobacteria*, *Gammaproteobacteria*, and *Deltaproteobacteria* of the Sva0485 clade. Further details of the
418 microbial community composition are given in von Hoyningen-Huene et al. (2019).



419

420 **Figure 11: Most abundant taxa in Core 01 (A) and Core 02 (B). The legend indicates all abundant taxa on the phylum**
 421 **level, including the class level for Proteobacteria and Firmicutes. All orders below 0.5% relative abundance were**
 422 **summarized as rare taxa. The abundant taxa change at the transitions from water column to sediment and the**
 423 **lithological units (I-III). The taxonomic composition of sulfate reducers in Core 01 (C) and Core 02 (D) changes**
 424 **gradually from Unit I to II and more pronouncedly from Unit II to III. Sulfate reducers are shown on the class and**
 425 **order level. The column thickness relates to the sampled increments of either 5 or 2.5 cm. Sulfate reducers represent up**
 426 **to 15% of the total bacterial community and were normalized to 100% relative abundance to illustrate the changes**
 427 **within their composition**

428



429 5. Discussion

430 5.1 Pore water gradients and their effect on Ca-Mg carbonate supersaturation

431 Concentrations of the conservative trending ions Na^+ , K^+ , and Cl^- , steadily increase towards the bottom of the core
 432 section, reaching 19, 1, and 9 $\text{mmol}\cdot\text{L}^{-1}$, respectively. These concentrations are considerably higher than in the
 433 water column, where these ions measure 14, 0.9 and 7 $\text{mmol}\cdot\text{L}^{-1}$. Moreover, SO_4^{2-} shows an increase near the
 434 bottom of the core and is reported to further increase to values of 6.5 $\text{mmol}\cdot\text{L}^{-1}$ in a longer section from a different
 435 locality in the Bay of Rust (not shown in this study), which is higher than the overlying lake water (3.9 $\text{mmol}\cdot\text{L}^{-1}$).
 436 This rise in ion concentration indicates an ion source below the sampled interval. While saline deep ground
 437 waters are known to be present in deep aquifers (Neuhuber, 1971; Blohm, 1974; Wolfram, 2006), it is also possible
 438 that more highly concentrated brine exists in deeper mud layers due to more recent evaporation events (Fig. 12).
 439 Lake Neusiedl dried out entirely between 1865 and 1875 (Moser, 1866) and high ion concentrations may relate to
 440 thin evaporite layers and brines that formed during this event.

441 The cause of the exceptionally high Mg:Ca ratio, which reaches values around 15 in the water column, is not yet
 442 entirely understood. The low Ca^{2+} concentrations in Lake Neusiedl can be linked to calcium carbonate formation
 443 (e.g. Wolfram and Herzig, 2013), but the for oligohaline, soda-type lakes uncommonly high amounts of Mg^{2+} ions
 444 and their source remain elusive. Boros et al. (2014) describe similar phenomena in small alkaline lakes of the
 445 western Carpathian plain and relate the high magnesium levels to local hydrogeological conditions and the
 446 geological substrate of the lakes.

447 It should be noted that the Mg:Ca ratio reaches values around 7 in the 5-10 cm increment of the pore water section.
 448 This is caused by a considerable decrease of the Mg^{2+} ions in this increment (from 5 to 4 $\text{mmol}\cdot\text{L}^{-1}$) and an increase
 449 in Ca^{2+} concentration (from 0.3 to 0.5 $\text{mmol}\cdot\text{L}^{-1}$). This effect can be partly explained by a transition zone between
 450 lake and pore water in this section, in which the concentration gradient is balanced. Other factors contributing to
 451 this concentration shift may include ion exchange, e.g. with NH_4^+ generated in the pore water at clay minerals (von
 452 Breymann et al., 1990; Celik et al., 2001). However, in the case of Lake Neusiedl, the NH_4^+ concentration is not
 453 sufficient to explain this change within the Mg:Ca ratio. Another factor causing the decrease of Mg^{2+}
 454 concentrations may be the supply of dissolved silica for the precipitation of clay mineral precursor phases (Birsoy,
 455 2002). Increasing SiO_2 concentration with depth indicates the dissolution of diatom frustules, which have been
 456 observed in thin sections of the present study. It is not entirely clear if this SiO_2 release into the pore water is
 457 related to hydrochemical or biogenic parameters. As the SiO_2 increase in the upper 20 cm of the pore water neither
 458 clearly correlates with alkalinity, nor with the salinity gradients (concentrations of conservative ions) and pH is
 459 not predictive (Ryves et al., 2006), diatom dissolution by an evident chemical undersaturation (saturation indices
 460 of amorphous SiO_2 lie between -1.35 and -0.65) may be not the only driver for the SiO_2 release. It is also
 461 conceivable that the enhanced silica release in the pore water is caused by bacteria, which attack the organic matrix
 462 of diatom frustules and, thus, expose the silica bearing skeletons to chemical undersaturation (Bidle and Azam,
 463 1999). Bidle et al. (2003) have linked enhanced dissolution potential to uncultured *Gammaproteobacteria*. This
 464 phylum showed increased abundances in the upper sediment column, supporting the hypothesis of a biogenic
 465 contribution to diatom dissolution and, hence, the provision of SiO_2 to sequester Mg^{2+} (Fig. 12, eq. (5)) in Lake
 466 Neusiedl's pore waters.

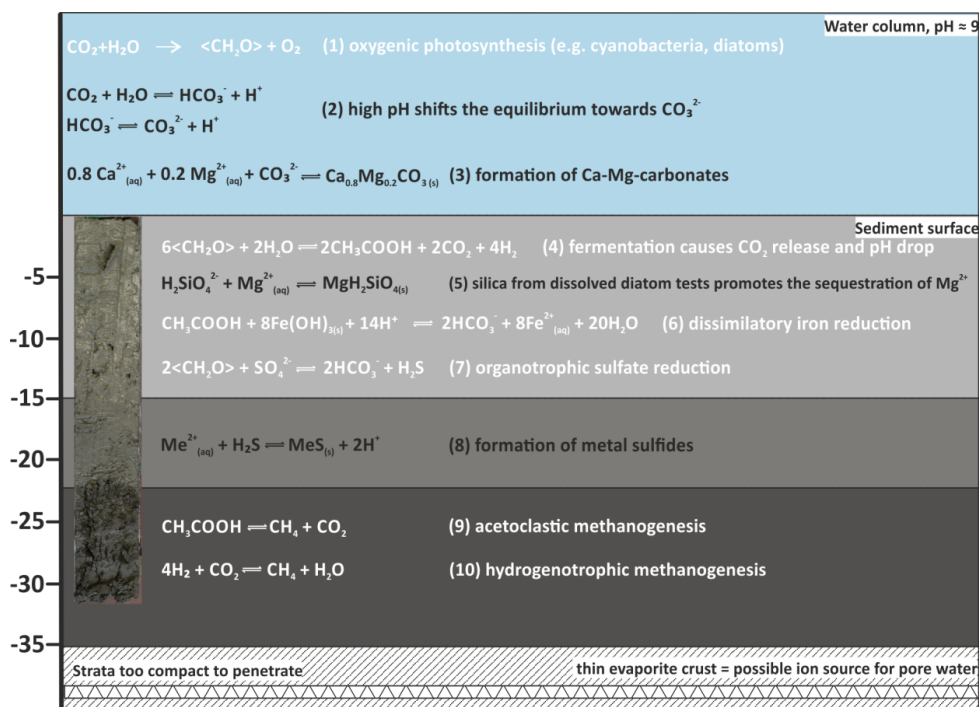


Figure 12: Suggested major microbial (simplified, indicated in white) and geochemical processes in water- and sediment column of Lake Neusiedl.

5.2 Microbial activity and carbonate saturation

Microbial metabolic reactions strongly affect pore water chemistry, particularly pH, alkalinity and hence carbonate mineral saturation state. In the present approach, the assessment of bacterial community composition is based on the metagenomic DNA within the sediment. This contains the active bacterial communities at their current depth as well as deposited, dormant or dead cells that originated in the water column or at shallower sediment depth (More et al., 2019). In the present study, a background of dormant or dead cells is evident through ASVs belonging to strict aerobes (e.g. *Rhizobiales*, *Gaiellales*) that were detected within deeper parts of the anaerobic mud core (Fig. 11; Suppl. Material Tab. S5).

The water column is characterized by aerobic heterotrophs, including C1-oxidizers (SAR11 clade of the *Alphaproteobacteria*) and highly abundant freshwater *Actinobacteria*. These are common in most freshwater environments. An impact on carbonate mineral saturation or nucleation, however, is unknown as their role in the biogeochemical cycles remains largely undescribed (Neuenschwander, et al., 2018). A high abundance of *Cyanobacteria* of the *Synechococcales* is present in the water column. *Synechococcales* are known to create favorable conditions for carbonate nucleation in alkaline environments by raising the pH, photosynthetic metabolism and the complexation of cations at their cell envelopes (Thompson and Ferris, 1990). Further research is required to verify their potential role in HMC or VHMC formation in Lake Neusiedl.

In sediment unit I (0-15 cm b. s.) *Synechococcales*, as well as aerobic *Bacteroidetes* are still abundant in the top 5 cm, likely due to the sedimentation of their cells from the water column. The uppermost measurement at 2.5 cm depth revealed reducing conditions and a low, close to neutral pH. This supports heterotrophic metabolisms and



489 fermentation by *Gammaproteobacteria*, *Acidobacteria*, *Chloroflexi*, and *Deltaproteobacteria*, which are the major
 490 taxa at this depth. At the very top of the sediment, a peak in NO_2^- and Fe^{2+} points to nitrate-reduction and Fe^{3+} -
 491 reduction (Kotlar et al., 1996; Jørgensen and Kasten, 2006). Farther below, the successive increase in NH_4^+ and
 492 PO_4^{3-} reflects anaerobic bacterial decomposition of organics, consistent e.g. with *Chloroflexi* capable of
 493 dissimilatory nitrate reduction to ammonium (DNRA).
 494 Sulfate-reducers are present in unit I. Their increasing relative abundance coincides with a decrease in SO_4^{2-} and
 495 an increase in $\Sigma\text{H}_2\text{S}$ (Fig. 9). Despite a concomitant increase in alkalinity, the bulk metabolic effect of the microbial
 496 community keeps the pH and carbonate saturation low (Fig. 12, eq (7)). Model calculations in aquatic sediments
 497 have shown that sulfate reduction initially lowers the pH (e.g. Soetart et al., 2007) and as the alkalinity increases,
 498 the pH converges at values between 6 and 7. As a consequence, the saturation index for carbonate minerals
 499 concomitantly drops. If a sufficient amount of sulfate is reduced ($>10 \text{ mmol}\cdot\text{L}^{-1}$), the saturation level recovers and
 500 may slightly surpass initial conditions (Meister, 2013). Only when sulfate reduction is coupled to anaerobic
 501 oxidation of methane (AOM), the effect of both would raise the pH to higher values. However, as methane occurs
 502 below 10 cm (Fig. 10), where SO_4^{2-} is still present, AOM is incomplete or absent.
 503 In sediment unit II (15-22 cm b. s.) and unit III (22-40 cm b. s.), the bacterial community composition shifts
 504 towards a high abundance of *Chloroflexi* (*Dehalococcoidia* and *Anaerolineae*), known for their involvement in
 505 carbon cycling as organohalide respirers and hydrocarbon degraders (Hug et al., 2013). This change may reflect
 506 an increase in poorly degradable organic electron donors and hence plant debris in the laminated core unit III. The
 507 change in the relative composition of different orders within the SRB (i.e., change from *Desulfobacterales* and
 508 *Desulfarculales* to Sva0485 and *Spirochaetales*) may also be related to a change in available organic substrates.
 509 In total, sulfate reduction remains high, also recognizable by the occurrence of opaque (sulfide-) mineral spots and
 510 the increase of S_{tot} in the lower part of the section (Fig. 2E; Fig. 3). Fermentation as well as sulfate-reduction
 511 remain high with increasing depth, indicated by the near-neutral pH and raised alkalinity at low carbonate mineral
 512 saturation.

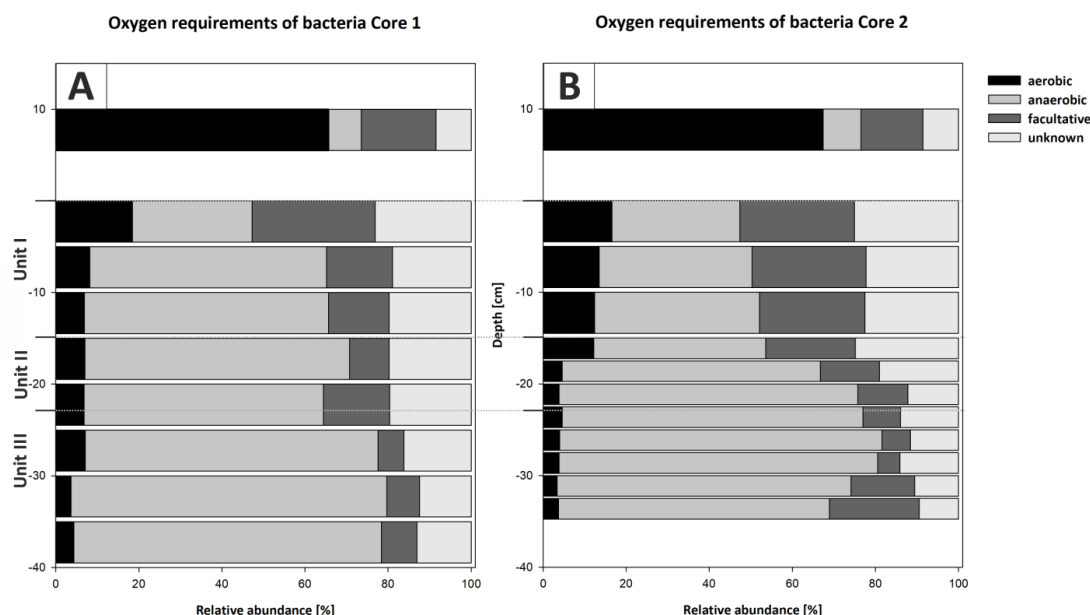


Figure 13: Oxygen utilization within the most abundant members of the bacterial community (A) and the potential energy metabolisms (B) plotted versus depth in Cores 01 and 02. The community in the water column indicates a predominantly aerobic regime. Rare taxa (< 0.5% relative abundance) were removed from the analysis and abundances normalized to 100%. Bacteria with an unknown metabolism were grouped as unknowns. The community inhabiting the sediment shows an early onset of sulfate reduction in the upper sediment layers and a shift to fermentation at the transition from Unit II to Unit III.

5.3 Time and depth of carbonate formation

A significant difference in saturation state between the water column and the sediment is evident. Whilst the water column is supersaturated with respect to aragonite, HMC, VHMC and dolomite, they are close to equilibrium in the pore water. The down shift of saturation from the water column to the pore water is to be expected, due to the onset of anaerobic, heterotrophic metabolic activity (Fig. 12, eq (4)).

The absence of aragonite at Lake Neusiedl is not entirely clear, as its formation is commonly linked to an interplay between high temperature, mineral supersaturation and Mg:Ca ratios (Fernández-Díaz et al., 1996; Given and Wilkinson, 1985). Based on precipitation experiments by De Choudens-Sanchez and Gonzalez (2009), which include temperatures of 19.98 °C and Mg:Ca ratios up to 5, aragonite would be the favored phase in Lake Neusiedl, as the lake's Mg:Ca ratio of 15 is too high and the concomitant calcite saturation not sufficient to provide calcite growth. However, the mentioned experiments were performed in a precipitation chamber with degassing conditions and hence reduced $p\text{CO}_2$, which makes them incomparable to the present study. In contrast, Niedermayr et al. (2013) observed the preferential formation of calcite at high Mg:Ca ratios when an amino acid (polyaspartic acid) is present. As the water column bears numerous bacterial species (Fig. 11) and potentially comparable organic compounds, this is a likely scenario for Lake Neusiedl. Nevertheless, the precise evaluation why aragonite, is not present is impossible, as no related analytical data from the water column are available.

According to Löffler (1979), magnesium calcite forms first, which then alters to protodolomite/VHMC. The alteration takes place from the inside, hence, resulting in a VHMC core and a HMC rim. However, the observation



that ratios of HMC to VHMC remain constant around 40 to 50% indicates no significant diagenetic alteration in the uppermost 30 cm of the sediment. Abrupt changes in these ratios, along with changing contributions of detrital mineral phases, such as mica and quartz, rather suggest changing sedimentation. Likewise, (low-Mg-) calcite essentially depends on the input of ostracod shells and transport of detrital carbonates delivered from the catchment area. Furthermore, no significant diagenetic overprint in form of recrystallization and/or cementation is apparent from the applied light- and electron-optical methods as well as the geochemical gradients. Most importantly, the stoichiometric ratio of each carbonate phase remains constant, confirming that no large-scale recrystallization of these phases occurs.

Considering that no signs of carbonate precipitation or diagenetic alteration were observed in the sediment column from the Bay of Rust, it can be concluded that carbonate minerals are unlikely to form in the pore water. Instead Ca-Mg carbonate crystals may precipitate in the water column and are deposited at the bottom of the lake (Fig. 12, eq (3)). Age estimations for the mud sediments range from 150 years (Löffler, 1979) to 850-2300 years before present (radiocarbon ages from Neuhuber et al., 2015). Our dataset indicates that authigenic Ca-Mg Carbonate does not necessarily form in its present location, which is consistent with the large discrepancy between sediment- and authigenic carbonate age.

The observed detrital mineral spectrum reflects the mineral composition of the adjacent Leitha- (mica, feldspar, quartz, calcite) and Rust Hills (calcite) and are either windblown or transported by small, eastbound tributaries (Löffler, 1979). The layering in the lower part of the section (Unit III) reflects the lack of homogenization by wind driven wave action and indicates a higher water level. As this unit also contains higher amounts of plant particles and siliciclastics, possibly due to a higher water influx from vegetated surroundings, it is conceivable that the deposition of Unit III reflects environmental conditions before the installation of the water level regulating Einsers-Kanal in 1909. The increase of C_{org} with depth further reflects this depositional change. It fits the increasing amount of plant particles with depth. The lignin bearing plant particles are difficult to degrade for heterotrophic organisms under the prevailing anoxic conditions (Benner et al., 1984). The higher amounts of plant material may reflect a lower salinity and thus higher primary production at their time of deposition, which can also be related to the stronger water level oscillations before regulations, including a larger lake surface and almost a magnitude higher catchment area (refer to a map in the supplementary data, provided by Hegedüs (1783)). Based on this consideration one might concur with the sediment age estimation of circa 150 years, as proposed by Löffler (1979). Nevertheless, it is important to distinguish between actual mineral formation and sediment deposition, including relocation: An unpublished sediment thickness map (GeNeSee project; unpubl.) suggests a current-driven relocation of mud deposits in the south-western lake area, where the bay of Rust is located. Thus, the radiocarbon data from Neuhuber et al. (2015) possibly reflect the date of precipitation, whereas Löffler's age estimation may refer to the date of local mud deposition.

571

572 **5.4 Potential pathways of authigenic Ca-Mg carbonate formation**

The precise formation pathway of authigenic Ca-Mg carbonate mineral precipitation in Lake Neusiedl has been controversially discussed. Some authors suggest a precipitation of HMC in the water column and subsequent alteration to VHMC or dolomite within the anoxic pore water of the sediment (Müller et al., 1972). Others suggest the direct formation of VHMC in the water column (Schiemer and Weisser, 1972). Our XRD and geochemical data support the latter hypothesis, as no diagenetic alteration is retraceable throughout the sediment section. While low saturation or even undersaturation in the sediment precludes a microbially induced precipitation in the pore



579 water, high supersaturation in the surface water body would support precipitation in the water column. Given the
 580 high alkalinity, CO₂ uptake by primary producers may have contributed to the high pH and high supersaturation
 581 in the surface water.

582 An alternative explanation to the controversially discussed microbial dolomite formation would be the ripening
 583 under fluctuating pH conditions in the water column. Deelman (1999) has demonstrated in his precipitation
 584 experiments that dolomite forms if the pH varies. At times of strong supersaturation, metastable carbonates
 585 (protodolomite) are formed, which ripen to ordered dolomite during subsequent phases of undersaturation of the
 586 metastable carbonate (while the stable phase remains supersaturated). This observation reflects Ostwald's step
 587 rule, according to which the metastable phase always forms first. Ostwald's step rule can also be demonstrated in
 588 the pore water, which is buffered by the metastable phase. Thereby the formation of the stable phase (dolomite) is
 589 inhibited despite its supersaturation. This observation is comparable with Land's (1998) "failure" to form dolomite
 590 for 30 years despite 1000-fold supersaturation.

591 In Lake Neusiedl, fluctuation of the pH in the overlying water column is likely to occur due to variations in
 592 meteoric water input and temperature, which may cause episodes of undersaturation. A fact, which is supported
 593 by Wolfram and Herzig (2013), who report an increase of Ca²⁺ concentration, depending on a dissolution of Ca-
 594 carbonates in Lake Neusiedl's open water during the winter months, when water levels rise and temperatures
 595 decrease. Such a seasonal dependent formation mechanism has recently been suggested to explain dolomite
 596 formation in a Triassic evaporative tidal flat setting (Meister and Frisia, 2019). Alternatively, Moreira et al. (2004)
 597 proposed that undersaturation of metastable phases occurs as a result of sulfide oxidation near the sediment surface.
 598 While we traced only small abundances of sulfate-oxidizing bacteria near the sediment-water interface (1%),
 599 fluctuating hydro-chemical conditions are likely to occur in the diffusive boundary layer, where a pH drop is
 600 observed as a result of the biogeochemical processes discussed above. Dolomite formation in the diffusive
 601 boundary layer has been observed in Lake Van (McCormack et al., 2018), and was interpreted as a result of
 602 abundant microbial EPS, linked to a changing water level and hence -chemistry. In Lake Neusiedl, the amount of
 603 EPS in the diffusive boundary layer is difficult to estimate, but the potential Ca-Mg carbonate favoring change in
 604 hydrochemistry is granted.

605 6. Conclusions

606 Two phases of Ca-Mg carbonates (HMC, VHMC) as well as calcite occur in form of fine-grained mud in Lake
 607 Neusiedl. Bacterial metabolic activity, including sulfate reduction and fermentation, leads to a decrease of pH
 608 within the sediment, leaving the Ca-Mg-carbonate phases at low/minor saturation in the pore water. In contrast,
 609 Ca-Mg carbonate phases are highly supersaturated in the alkaline water column. There, the carbonate formation
 610 mechanism may involve fluctuating hydrochemical conditions, leading to periods of undersaturation and ripening
 611 of HMC to VHMC. Further, carbonate precipitation may be supported by phototrophic uptake of CO₂ by
 612 cyanobacteria, e.g. by *Synechococcus*. Precipitation of Ca-Mg carbonate, thus, most likely occurs in the open water.
 613 Based on the presented data set, precipitation or diagenetic alteration within the sediment is not indicated. The
 614 precise Ca-Mg carbonate reaction pathway needs further evaluation.



615 **Data availability**

616 All data required for the presented plots and supplementary, analytical data were submitted to PANGEA (Data
617 Publisher for Earth & Environmental Science, doi to be assigned). Microbiological datasets can be requested from
618 Avril von Hoyningen-Huene.

619 **Author contributions**

620 Dario Fussmann, Patrick Meister and Andreas Reimer investigated, formally analyzed and curated the hydro- and
621 geochemical data. Avril Jean Elisabeth von Hoyningen-Huene investigated the bacterial communities, and
622 formally analysed and curated the data together with Dominik Schneider and Dario Fussmann. Hana Babková,
623 Andreas Maier and Robert Peticzka conducted data curation. Dario Fussmann wrote the original draft, which was
624 reviewed and edited by Patrick Meister, Avril Jean Elisabeth von Hoyningen-Huene, Andreas Reimer, Dominik
625 Schneider, Gernot Arp and Rolf Daniel. Gernot Arp and Rolf Daniel conceptualized the study, acquired the
626 funding, administered and supervised the project.

627 **Competing interests**

628 The authors declare that they have no conflict of interest.

629 **Acknowledgements**

630 We thank Wolfgang Dröse, Birgit Röring, and Axel Hackmann for their support during lab work. Furthermore,
631 we thank Susanne Gier for support during XRD measurements and Beatrix Bethke, Caroline Haberhauer, and
632 Barbara Hofbauer for help during sampling. We also thank Erich Draganits, Regina and Rudolf Krachler, and
633 Stephanie Neuhuber for insightful discussions.

634 **Financial support**

635 The project was funded by the German Research Foundation DFG, research unit FOR-1644 "CHARON"
636 (subproject TP7: AR 335/8-1, DA 374/11-1). Further support was provided by the Open Access Publication Funds
637 of the Göttingen University. P.M. received funding by the European Commission (Marie-Curie IEF Project
638 TRIADOL; no. 626025) and by the Department of Geodynamics and Sedimentology at the University of Vienna.

639



640 References

- 641 Alderkamp, A.-C., Nejstgaard, J. C., Verity, P. G., Zirbel, M. J., Sazhin, A. F., and van Rijssel, M.: Dynamics in
 642 carbohydrate composition of *Phaeocystis pouchetii* colonies during spring blooms in mesocosms, *Journal*
 643 *of Sea Research*, 55, 169, <https://doi.org/10.1016/j.seares.2005.10.005>, 2006.
- 644 Aloisi, G.: The calcium carbonate saturation state in cyanobacterial mats throughout Earth's history, *Geochimica*
 645 *et Cosmochimica Acta*, 72, 6037, <https://doi.org/10.1016/j.gca.2008.10.007>, 2008.
- 646 Bácsatyai, L., Csaplovics, E., Márkus, I. and Sindhuber, A.: Digitale Geländemodelle des Neusiedler See-Beckens,
 647 *Wissenschaftliche Arbeiten aus dem Burgenland*, 97, 1997
- 648 Balci, N., Menekşe, M., Karagüler, N. G., Şeref Sönmez, M., and Meister, P.: Reproducing authigenic carbonate
 649 precipitation in the hypersaline Lake Acıgöl (Turkey) with microbial cultures, *Geomicrobiology journal*,
 650 33, 758, <https://doi.org/10.1080/01490451.2015.1099763>, 2016.
- 651 Benner, R., Maccubbin, A., and Hodson, R. E.: Anaerobic biodegradation of the lignin and polysaccharide
 652 components of lignocellulose and synthetic lignin by sediment microflora, *Appl. Environ. Microbiol.*, 47,
 653 998, 1984.
- 654 Bidle, K. D., and Azam, F.: Accelerated dissolution of diatom silica by marine bacterial assemblages, *Nature*, 397,
 655 508, <https://doi.org/10.1038/17351>, 1999.
- 656 Bidle, K. D., Brzezinski, M. A., Long, R. A., Jones, J. L., and Azam, F.: Diminished efficiency in the oceanic
 657 silica pump caused by bacteria-mediated silica dissolution, *Limnology and Oceanography*, 48, 1855,
 658 <https://doi.org/10.4319/lo.2003.48.5.1855>, 2003.
- 659 Birgel, D., Meister, P., Lundberg, R., Horath, T. D., Bontognali, T.R., Bahniuk, A. M., de Rezende, C. E.,
 660 Vasconcelos, C. and McKenzie, J. A.: Methanogenesis produces strong ^{13}C enrichment in stromatolites
 661 of Lagoa Salgada, Brazil: a modern analogue for Palaeo-/Neoproterozoic stromatolites?, *Geobiology*, 13,
 662 3, <https://doi.org/10.1111/gbi.12130>, 2015
- 663 Birsoy, R.: Formation of sepiolite-palygorskite and related minerals from solution, *Clays and Clay Minerals*, 50,
 664 736, <https://doi.org/10.1346/000986002762090263>, 2002.
- 665 Blohm, M.: Sedimentpetrographische Untersuchungen am Neusiedler See, Österreich, na, 1974.
- 666 Bontognali, T. R., Vasconcelos, C., Warthmann, R. J., Dupraz, C., Bernasconi, S. M., and McKenzie, J. A.:
 667 Microbes produce nanobacteria-like structures, avoiding cell entombment, *Geology*, 36, 663,
 668 <https://doi.org/10.1130/g24755a.1>, 2008.
- 669 Bontognali, T. R., Vasconcelos, C., Warthmann, R. J., Bernasconi, S. M., Dupraz, C., Strohmenger, C. J., and
 670 McKenzie, J. A.: Dolomite formation within microbial mats in the coastal sabkha of Abu Dhabi (United
 671 Arab Emirates), *Sedimentology*, 57, 824, <https://doi.org/10.1111/j.1365-3091.2009.01121.x>, 2010.
- 672 Bontognali, T. R., McKenzie, J. A., Warthmann, R. J., and Vasconcelos, C.: Microbially influenced formation of
 673 Mg-calcite and Ca-dolomite in the presence of exopolymeric substances produced by sulphate-reducing
 674 bacteria, *Terra Nova*, 26, 72, <https://doi.org/10.1111/ter.12072>, 2014.
- 675 Boros, E., Horváth, Z., Wolfram, G., and Vörös, L.: Salinity and ionic composition of the shallow astatic soda
 676 pans in the Carpathian Basin, *Annales de Limnologie-International Journal of Limnology*, 59,
 677 <https://doi.org/10.1051/limn/2013068>, 2014
- 678 Brady, P.V., Krumhansl, J. L. and Papenguth, H.W.: Surface complexation clues to dolomite growth, *Geochemica*
 679 *et Cosmochemica Acta*, 60, 4, [https://doi.org/10.1016/0016-7037\(95\)00436-x](https://doi.org/10.1016/0016-7037(95)00436-x), 1996



- 680 Callahan, B. J., McMurdie, P. J., and Holmes, S. P.: Exact sequence variants should replace operational taxonomic
 681 units in marker-gene data analysis, *The ISME journal*, 11, 2639, <https://doi.org/10.1038/ismej.2017.119>,
 682 2017.
- 683 Celik, M., Özdemir, B., Turan, M., Koyuncu, I., Atesok, G., and Sarikaya, H.: Removal of ammonia by natural
 684 clay minerals using fixed and fluidised bed column reactors, *Water Science and Technology: Water*
 685 *Supply*, 1, 81, <https://doi.org/10.2166/ws.2001.0010>, 2001.
- 686 Chen, S., Zhou, Y., Chen, Y., and Gu, J.: fastp: an ultra-fast all-in-one FASTQ preprocessor, *Bioinformatics*, 34,
 687 i884, <https://doi.org/10.1093/bioinformatics/bty560>, 2018.
- 688 Chiang, E., Schmidt, M. L., Berry, M. A., Biddanda, B. A., Burtner, A., Johengen, T. H., Palladino, D., and Deneff,
 689 V. J.: Verrucomicrobia are prevalent in north-temperate freshwater lakes and display class-level
 690 preferences between lake habitats, *PLoS One*, 13, e0195112,
 691 <https://doi.org/10.1371/journal.pone.0195112>, 2018.
- 692 Court, W. M., Paul, A., and Lokier, S. W.: The preservation potential of environmentally diagnostic sedimentary
 693 structures from a coastal sabkha, *Marine Geology*, 386, 1, <https://doi.org/10.1016/j.margeo.2017.02.003>,
 694 2017.
- 695 Daye, M., Higgins J. and Bosak, T.: Formation of ordered dolomite in anaerobic photosynthetic biofilms. *Geology*,
 696 47, 509-512, <https://doi.org/10.1130/g45821.1>, 2019.
- 697 De Choudens-Sanchez, V. and Gonzalez, L. A.: Calcite and aragonite precipitation under controlled instantaneous
 698 supersaturation: elucidating the role of CaCO₃ saturation state and Mg/Ca ration on calcium carbonate
 699 polymorphism. *Journal of Sedimentary Research*, 79, 363-376, <https://doi.org/10.2110/jsr.2009.043>,
 700 2009.
- 701 Deelman, J.: Low-temperature nucleation of magnesite and dolomite, *Neues Jahrbuch Fur Mineralogie*
 702 *Monatshefte*, 289, 1999.
- 703 Deng, S., Dong, H., Lv, G., Jiang, H., Yu, B., and Bishop, M. E.: Microbial dolomite precipitation using sulfate
 704 reducing and halophilic bacteria: Results from Qinghai Lake, Tibetan Plateau, NW China, *Chemical*
 705 *Geology*, 278, 151, <https://doi.org/10.1016/j.chemgeo.2010.09.008>, 2010.
- 706 Flombaum, P., Gallegos, J. L., Gordillo, R. A., Rincón, J., Zabala, L. L., Jiao, N., Karl, D. M., Li, W. K., Lomas,
 707 M. W., and Veneziano, D.: Present and future global distributions of the marine Cyanobacteria
 708 *Prochlorococcus* and *Synechococcus*, *Proceedings of the National Academy of Sciences*, 110, 9824,
 709 <https://doi.org/10.1073/pnas.1307701110>, 2013.
- 710 Frisia, S., Borsato, A., and Hellstrom, J.: High spatial resolution investigation of nucleation, growth and early
 711 diagenesis in speleothems as exemplar for sedimentary carbonates, *Earth-Science Reviews*, 178, 68,
 712 <https://doi.org/10.1016/j.earscirev.2018.01.014>, 2018.
- 713 Grasshoff, K., Kremling, K., and Ehrhardt, M.: *Methods of seawater analysis*, John Wiley & Sons,
 714 <https://doi.org/10.1002/9783527613984>, 2009.
- 715 Gregg, J. M., Bish, D. L., Kaczmarek, S. E., and Machel, H. G.: Mineralogy, nucleation and growth of
 716 dolomite in the laboratory and sedimentary environment: a review, *Sedimentology*, 62, 1749,
 717 <https://doi.org/10.1111/sed.12202>, 2015.
- 718 Hahnke, R. L., Meier-Kolthoff, J. P., García-López, M., Mukherjee, S., Huntemann, M., Ivanova, N. N., Woyke,
 719 T., Kyrpides, N. C., Klenk, H.-P., and Göker, M.: Genome-based taxonomic classification of
 720 Bacteroidetes, *Frontiers in microbiology*, 7, 2003, <https://doi.org/10.3389/fmicb.2016.02003>, 2016.



- 721 He, S., Stevens, S. L., Chan, L.-K., Bertilsson, S., del Rio, T. G., Tringe, S. G., Malmstrom, R. R., and McMahon,
 722 K. D.: Ecophysiology of freshwater Verrucomicrobia inferred from metagenome-assembled genomes,
 723 mSphere, 2, e00277, <https://doi.org/10.1128/msphere.00277-17>, 2017.
- 724 Hegedüs, J.N.: Lake Neusiedl and Hansag: Universal map of the County of Sopron, State archive of Sopron, 1783
- 725 Herrmann, P., Pascher, G., and Pistonik, J.: Geologische Karte der Republik Österreich. Geologische
 726 Bundesanstalt, Wien, 1993.
- 727 Herzig, A.: Der Neusiedler See - Limnologie eines Steppensees, Denisia 33, zugleich Kataloge des
 728 oberösterreichischen Landesmuseums, 163, 101-114, 2014
- 729 Herzig, A., and Dokulil, M.: Neusiedler See - ein Steppensee in Europa., in: Ökologie und Schutz von Seen., edited
 730 by: Dokulil, M., Hamm, A., and Kohl, J.-G., Facultas-Universitäts-Verlag, Wien, 401, 2001
- 731 Holmkvist, L., Kamyshny Jr, A., Bruechert, V., Ferdelman, T. G., and Jørgensen, B. B.: Sulfidization of lacustrine
 732 glacial clay upon Holocene marine transgression (Arkona Basin, Baltic Sea), Geochimica et
 733 Cosmochimica Acta, 142, 75, <https://doi.org/10.1016/j.gca.2014.07.030>, 2014.
- 734 Horváth, F.: Towards a mechanical model for the formation of the Pannonian basin, Tectonophysics, 226, 333,
 735 [https://doi.org/10.1016/0040-1951\(93\)90126-5](https://doi.org/10.1016/0040-1951(93)90126-5), 1993.
- 736 Hug, L. A., Castelle, C. J., Wrighton, K. C., Thomas, B. C., Sharon, I., Frischkorn, K. R., Williams, K. H., Tringe,
 737 S. G., and Banfield, J. F.: Community genomic analyses constrain the distribution of metabolic traits
 738 across the Chloroflexi phylum and indicate roles in sediment carbon cycling, Microbiome, 1, 22,
 739 <https://doi.org/10.1186/2049-2618-1-22>, 2013
- 740 Illing, L., Wells, A., and Taylor, J.: Penecontemporary dolomite in the Persian Gulf, 1965.
- 741 Jørgensen, B. B., and Kasten, S.: Sulfur cycling and methane oxidation, in: Marine geochemistry, Springer, 271,
 742 https://doi.org/10.1007/3-540-32144-6_8, 2006.
- 743 Kampbell, D., Wilson, J. T., and Vandegrift, S.: Dissolved oxygen and methane in water by a GC headspace
 744 equilibration technique, International Journal of Environmental Analytical Chemistry, 36, 249,
 745 <https://doi.org/10.1080/03067318908026878>, 1989.
- 746 Klindworth, A., Pruesse, E., Schweer, T., Peplies, J., Quast, C., Horn, M., and Glöckner, F. O.: Evaluation of
 747 general 16S ribosomal RNA gene PCR primers for classical and next-generation sequencing-based
 748 diversity studies, Nucleic acids research, 41, e1, <https://doi.org/10.1093/nar/gks808>, 2013.
- 749 Kotlar, E., Tartakovsky, B., Argaman, Y., and Sheintuch, M.: The nature of interaction between immobilized
 750 nitrification and denitrification bacteria, Journal of biotechnology, 51, 251,
 751 [https://doi.org/10.1016/s0168-1656\(96\)01603-3](https://doi.org/10.1016/s0168-1656(96)01603-3), 1996.
- 752 Krachler, R., Korner, I., Dvorak, M., Milazowszky, N., Rabitsch, W., Werba, F., Zulka, P., and Kirschner, A.: Die
 753 Salzlacken des Seewinkels: Erhebung des aktuellen ökologischen Zustandes sowie Entwicklung
 754 individueller Lackenerhaltungskonzepte für die Salzlacken des Seewinkels (2008–2011), Krachler R,
 755 Kirschner A & Korner I (Redaktion). Verlag & Hrsg. Österreichischer Naturschutzbund, Eisenstadt,
 756 Österreich, 2012.
- 757 Krachler, R., Krachler, R., Gülce, F., Keppler, B. K., and Wallner, G.: Uranium concentrations in sediment pore
 758 waters of Lake Neusiedl, Austria, Science of the Total Environment, 633, 981,
 759 <https://doi.org/10.1016/j.scitotenv.2018.03.259>, 2018.
- 760 Land, L. S.: Failure to Precipitate Dolomite at 25 C from Dilute Solution Despite 1000-Fold Oversaturation after 32
 761 Years, Aquatic Geochemistry, 4, 361, 1998.



- 762 Lippmann, F.: The System $\text{CaCO}_3\text{-MgCO}_3$, in: *Sedimentary Carbonate Minerals*, Springer, 148,
 763 https://doi.org/10.1007/978-3-642-65474-9_4, 1973.
- 764 Liu, D., Xu, Y., Papineau, D., Yu, N., Fan, Q., Qiu, X., and Wang, H.: Experimental evidence for abiotic formation
 765 of low-temperature proto-dolomite facilitated by clay minerals, *Geochimica et Cosmochimica Acta*, 247,
 766 83, <https://doi.org/10.1016/j.gca.2018.12.036>, 2019.
- 767 Löffler, H.: Neusiedlersee: The limnology of a shallow lake in central europe, in: *Monographiae Biologicae*,
 768 edited by: Löffler, H., Dr. W. Junk bv Publishers, The Hague, 1, [https://doi.org/10.1007/978-94-009-](https://doi.org/10.1007/978-94-009-9168-2)
 769 9168-2, 1979.
- 770 Lutterotti, L., Bortolotti, M., Ischia, G., Lonardelli, I., and Wenk, H.: Rietveld texture analysis from diffraction
 771 images, *Z. Kristallogr. Suppl.* 26, 125, https://doi.org/10.1524/zksu.2007.2007.suppl_26.125, 2007.
- 772 Machel, H. G.: Concepts and models of dolomitization: a critical reappraisal, *Geological Society, London*,
 773 *Special Publications*, 235, 7, <https://doi.org/10.1144/gsl.sp.2004.235.01.02>, 2004.
- 774 Martin, M.: Cutadapt removes adapter sequences from high-throughput sequencing reads, *EMBnet. journal*, 17,
 775 10, <https://doi.org/10.14806/ej.17.1.200>, 2011.
- 776 McCormack, J., Bontognali, T. R., Immenhauser, A., and Kwiecien, O.: Controls on cyclic formation of
 777 Quaternary early diagenetic dolomite, *Geophysical Research Letters*, 45, 3625,
 778 <https://doi.org/10.1002/2018gl077344>, 2018.
- 779 Meister, P., Reyes, C., Beaumont, W., Rincon, M., Collins, L., Berelson, W., Stott, L., Corsetti, F., and Nealson,
 780 K.H.: Calcium- and magnesium-limited dolomite precipitation at Deep Springs Lake, California,
 781 *Sedimentology*, 58, 1810–1830, <https://doi.org/10.1111/j.1365-3091.2011.01240.x>, 2011.
- 782 Meister, P.: Two opposing effects of sulfate reduction on carbonate precipitation in normal marine, hypersaline,
 783 and alkaline environments, *Geology*, 41, 499, <https://doi.org/10.1130/g34185.1>, 2013.
- 784 Meister, P. and Frisia, S.: Dolomite formation by nano-crystal aggregation in the Dolomia Principale of the Brenta
 785 Dolomites (Northern Italy). *Rivista Italiana di Paleontologia e Stratigrafia*, 125, 183-196, 2019.
- 786 More, K. D., Giosan, L., Grice, K., and Coolen, M. J.: Holocene paleodepositional changes reflected in the
 787 sedimentary microbiome of the Black Sea, *Geobiology*, 17, 436, <https://doi.org/10.1111/gbi.12338>,
 788 2019.
- 789 Moreira, N., Walter, L. M., Vasconcelos, C., McKenzie, J. A. and McCall, P.: Role of sulfide oxidation in
 790 dolomitization: Sediments and pore-water geochemistry of a modern hypersaline lagoon system.
 791 *Geology*, 32,701-704, <https://doi.org/10.1130/g20353.1>, 2004.
- 792 Moser, I.: Der abgetrocknete Boden des Neusiedler See's, *Jahrb. Geolog. Reichsanst.* 16, 338, 1866.
- 793 Müller, G., Irion, G., and Förstner, U.: Formation and diagenesis of inorganic Ca-Mg carbonates in the
 794 lacustrine environment, *Naturwissenschaften*, 59, 158, <https://doi.org/10.1007/bf00637354>,
 795 1972.
- 796 Neuenschwander, S. M., Ghai, R., Pernthaler, J. and Salcher, M. M.: Microdiversification in genome streamlined
 797 ubiquitous freshwater Actinobacteria, *The ISME Journal*, 12, 1, <https://doi.org/10.1038/ismej.2017.156>,
 798 2018
- 799 Neuhuber, F.: Ein Beitrag zum Chemismus des Neusiedler Sees, *Sitz. Ber. Österr. Akad. Wiss., math.-nat. Kl.*,
 800 *Abt. I*, 179, 225, 1971.
- 801 Neuhuber, S., Steier, P., Gier, S., Draganits, E., and Kogelbauer, I.: Radiogenic Carbon Isotopes in Authigenic
 802 Carbonate from Lake Neusiedl, Austria, *EGU General Assembly Conference Abstracts*, 2015.



- 803 Niedermayr, A., Köhler, S. J., and Dietzel, M.: Impacts of aqueous carbonate accumulation rate, magnesium and
 804 polyaspartic acid on calcium carbonate formation (6–40 °C), *Chemical Geology*, 340, 105,
 805 <https://doi.org/10.1016/j.chemgeo.2012.12.014>, 2013.
- 806 Parkhurst, D. L., and Appelo, C.: Description of input and examples for PHREEQC version 3: a computer
 807 program for speciation, batch-reaction, one-dimensional transport, and inverse geochemical
 808 calculations, US Geological Survey, 2328-7055, <https://doi.org/10.3133/tm6a43>, 2013.
- 809 Pau, M., and Hammer, Ø.: Sediment mapping and long-term monitoring of currents and sediment fluxes in
 810 pockmarks in the Oslofjord, Norway, *Marine Geology*, 346, 262,
 811 <https://doi.org/10.1016/j.margeo.2013.09.012>, 2013.
- 812 Piller, W. E., Harzhauser, M., and Mandic, O.: Miocene Central Paratethys stratigraphy—current status and future
 813 directions, *Stratigraphy*, 4, 2007.
- 814 Quast, C., Pruesse, E., Yilmaz, P., Gerken, J., Schweer, T., Yarza, P., Peplies, J., and Glöckner, F. O.: The
 815 SILVA ribosomal RNA gene database project: improved data processing and web-based tools, *Nucleic
 816 acids research*, 41, D590, <https://doi.org/10.1093/nar/gks1219>, 2012.
- 817 Rivadeneyra, M. a. A., Delgado, G., Soriano, M., Ramos-Cormenzana, A., and Delgado, R.: Precipitation of
 818 carbonates by *Nesterenkonia halobia* in liquid media, *Chemosphere*, 41, 617,
 819 [https://doi.org/10.1016/s0045-6535\(99\)00496-8](https://doi.org/10.1016/s0045-6535(99)00496-8), 2000.
- 820 Roberts, J. A., Bennett, P. C., González, L. A., Macpherson, G., and Milliken, K. L.: Microbial precipitation of
 821 dolomite in methanogenic groundwater, *Geology*, 32, 277, <https://doi.org/10.1130/g20246.2>, 2004.
- 822 Rognes, T., Flouri, T., Nichols, B., Quince, C., and Mahé, F.: VSEARCH: a versatile open source tool for
 823 metagenomics, *PeerJ*, 4, e2584, <https://doi.org/10.7717/peerj.2584>, 2016.
- 824 Rosen, M. R., Miser, D. E., Starcher, M. A., and Warren, J. K.: Formation of dolomite in the Coorong region,
 825 South Australia, *Geochimica et Cosmochimica Acta*, 53, 661, [https://doi.org/10.1016/0016-7037\(89\)90009-4](https://doi.org/10.1016/0016-7037(89)90009-4), 1989.
- 827 Ryves, D. B., Battarbee, R. W., Juggins, S., Fritz, S. C., and Anderson, N. J.: Physical and chemical predictors of
 828 diatom dissolution in freshwater and saline lake sediments in North America and West Greenland,
 829 *Limnology and Oceanography*, 51, 1355, <https://doi.org/10.4319/lo.2006.51.3.1355>, 2006.
- 830 Sánchez-Román, M., Vasconcelos, C., Warthmann, R., Rivadeneyra, M., McKenzie, J. A., and Swart, P.:
 831 Microbial dolomite precipitation under aerobic conditions: results from Brejo do Espinho Lagoon
 832 (Brazil) and culture experiments, *Perspectives in Carbonate Geology: A Tribute to the Career of Robert
 833 Nathan Ginsburg*, 41, 167, <https://doi.org/10.1002/9781444312065>, 2009.
- 834 Schiemer, F., and Weisser, P.: Zur Verteilung der submersen Makrophyten in der schilffreien Zone des
 835 Neusiedler Sees, *Sitzungsber. Österr. Akad. Wiss., Math.-nat. Kl.(I)*, 180, 87, 1972.
- 836 Schmidt, F., Koch, B. P., Goldhammer, T., Elvert, M., Witt, M., Lin, Y.-S., Wendt, J., Zabel, M., Heuer, V. B.,
 837 and Hinrichs, K.-U.: Unraveling signatures of biogeochemical processes and the depositional setting in
 838 the molecular composition of pore water DOM across different marine environments, *Geochimica et
 839 Cosmochimica Acta*, 207, 57, <https://doi.org/10.1016/j.gca.2017.03.005>, 2017.
- 840 Schmidt, M., Xeflide, S., Botz, R., and Mann, S.: Oxygen isotope fractionation during synthesis of CaMg-
 841 carbonate and implications for sedimentary dolomite formation, *Geochimica et Cosmochimica Acta*,
 842 69, 4665, <https://doi.org/10.1016/j.gca.2005.06.025>, 2005.



- 843 Schneider, D., Thürmer, A., Gollnow, K., Lugert, R., Gunka, K., Groß, U., and Daniel, R.: Gut bacterial
 844 communities of diarrheic patients with indications of Clostridioides difficile infection, Scientific data, 4,
 845 170152, <https://doi.org/10.1038/sdata.2017.152>, 2017.
- 846 Schneider, D., Wemheuer, F., Pfeiffer, B., and Wemheuer, B.: Extraction of total DNA and RNA from marine
 847 filter samples and generation of a cDNA as universal template for marker gene studies, in: Metagenomics,
 848 Springer, 13, https://doi.org/10.1007/978-1-4939-6691-2_2, 2017.
- 849 Schroll, E., and Wieden, P.: Eine rezente Bildung von Dolomit im Schlamm des Neusiedler Sees, Tscherma
 850 mineralogische und petrographische Mitteilungen, 7, 286, <https://doi.org/10.1007/bf01127917>, 1960.
- 851 Seeberg-Elverfeldt, J., Schlüter, M., Feseker, T. and Kölling, M.: Rhizon sampling of porewaters near the
 852 sediment-water interface of aquatic systems. Limnology and oceanography: Methods, 3, 8,
 853 <https://doi.org/10.4319/lom.2005.3.361>, 2005
- 854 Shotbolt, L.: Pore water sampling from lake and estuary sediments using Rhizon samplers. Journal of
 855 Paleolimnology, 44, 2, <https://doi.org/10.1007/s10933-008-9301-8>, 2010.
- 856 Soetaert, K., Hofmann, A. F., Middelburg, J. J., Meysman, F.J. and Greenwood, J.: Reprint of “The effect of
 857 biogeochemical processes on pH.”, Marine Chemistry, 106, 1-2,
 858 <https://doi.org/10.1016/j.marchem.2007.06.008>, 2007
- 859 Steiner, Z., Lazar, B., Erez, J., and Turchyn, A. V.: Comparing Rhizon samplers and centrifugation for pore-
 860 water separation in studies of the marine carbonate system in sediments, Limnology and Oceanography:
 861 Methods, 16, 828, <https://doi.org/10.1002/lom3.10286>, 2018.
- 862 Systat Software: SigmaPlot for Windows, version 11.0, 2008.
- 863 Team, R.: RStudio: integrated development for R.(RStudio, Inc., Boston, MA, USA), 2016.
- 864 Team, R. C.: R: A language and environment for statistical computing, 2018.
- 865 Thompson, J., and Ferris, F.: Cyanobacterial precipitation of gypsum, calcite, and magnesite from natural
 866 alkaline lake water, Geology, 18, 995,
 867 [https://doi.org/10.1130/00917613\(1990\)018<0995:cpogca>2.3.co;2](https://doi.org/10.1130/00917613(1990)018<0995:cpogca>2.3.co;2), 1990.
- 868 van Husen, D.: Quaternary glaciations in Austria, in: Developments in Quaternary Sciences, Elsevier, 1,
 869 [https://doi.org/10.1016/s1571-0866\(04\)80051-4](https://doi.org/10.1016/s1571-0866(04)80051-4), 2004.
- 870 van Lith et al. (2002) Bacterial sulfate reduction and salinity: two controls on dolomite precipitation in Lagoa
 871 Vermelha and Brejo do Espinho (Brazil) Hydrobiologia 485, 35–49,
 872 <https://doi.org/10.1007/s00792-005-0441-8>, 2002.
- 873 van Tuyl, F.M.: The origin of dolomite, Iowa Geol. Survey Ann. Rep, 25, 251-421, <https://doi.org/10.17077/2160-5270.1180>, 1914.
- 875 Vasconcelos, C., McKenzie, J. A., Bernasconi, S., Grujic, D., and Tiens, A. J.: Microbial mediation as a possible
 876 mechanism for natural dolomite formation at low temperatures, Nature, 377, 220,
 877 <https://doi.org/10.1038/377220a0>, 1995.
- 878 Vasconcelos, C., and McKenzie, J. A.: Microbial mediation of modern dolomite precipitation and diagenesis
 879 under anoxic conditions (Lagoa Vermelha, Rio de Janeiro, Brazil), Journal of sedimentary Research,
 880 67, 378, <https://doi.org/10.1306/d4268577-2b26-11d7-8648000102c1865d>, 1997.
- 881 von Breyman, M. T., Collier, R., and Suess, E.: Magnesium adsorption and ion exchange in marine sediments:
 882 A multi-component model, Geochimica et Cosmochimica Acta, 54, 3295,
 883 [https://doi.org/10.1016/0016-7037\(90\)90286-t](https://doi.org/10.1016/0016-7037(90)90286-t), 1990.



- 884 von der Borch, C. C., Lock, D. E., and Schwebel, D.: Ground-water formation of dolomite in the Coorong region
 885 of South Australia, *Geology*, 3, 283, [https://doi.org/10.1130/0091-7613\(1975\)3<283:gfodit>2.0.co;2](https://doi.org/10.1130/0091-7613(1975)3<283:gfodit>2.0.co;2),
 886 1975.
- 887 von Hoyningen-Huene, A. J. E., Schneider, D., Fussmann, D., Reimer, A., Arp, G., and Daniel, R.: Bacterial
 888 succession along a sediment porewater gradient at Lake Neusiedl in Austria, *Scientific data*, 6, 1,
 889 <https://doi.org/10.1038/s41597-019-0172-9>, 2019.
- 890 Warren, J. K.: Sedimentology and mineralogy of dolomitic Coorong lakes, South Australia, *Journal of*
 891 *sedimentary Research*, 60, 843, <https://doi.org/10.1306/212f929b-2b24-11d7-8648000102c1865d>,
 892 1990.
- 893 Wenk, H.-R., Hu, M., and Frisia, S.: Partially disordered dolomite: microstructural characterization of Abu
 894 Dhabi sabkha carbonates, *American Mineralogist*, 78, 769, 1993.
- 895 Whitman, W. B.: *Bergey's manual of systematics of Archaea and Bacteria*, Wiley Online Library, 2015.
- 896 Wickham, H.: *ggplot2: elegant graphics for data analysis*, Springer,
 897 https://doi.org/10.1007/978-3-319-24277-4_12, 2016.
- 898 Wolfram, G.: Bedeutung und Vorkommen von Salzlebensräumen, Wolfram, G., et al, 13, 2006.
- 899 Wright, D. T., and Wacey, D.: Precipitation of dolomite using sulphate-reducing bacteria from the Coorong
 900 Region, South Australia: significance and implications, *Sedimentology*, 52, 987,
 901 <https://doi.org/10.1111/j.1365-3091.2005.00732.x>, 2005.
- 902 Wolfram, G. and Herzig, A. (2013) Nährstoffbilanz Neusiedler See. *Wiener Mitteilungen*, 228, 317-338
- 903 Zámolyi, A., Salcher, B., Draganits, E., Exner, U., Wagreich, M., Gier, S., Fiebig, M., Lomax, J., Surányi, G.,
 904 and Diel, M.: Latest Pannonian and Quaternary evolution at the transition between Eastern Alps and
 905 Pannonian Basin: new insights from geophysical, sedimentological and geochronological data,
 906 *International Journal of Earth Sciences*, 106, 1695, <https://doi.org/10.1007/s00531-016-1383-3>, 2017.
- 907 Zhang, J., Kobert, K., Flouri, T., and Stamatakis, A.: PEAR: a fast and accurate Illumina Paired-End reAd
 908 mergeR, *Bioinformatics*, 30, 614, <https://doi.org/10.1093/bioinformatics/btt593>, 2013a.
- 909 Zhang, F., Yan, C., Teng, H.H., Roden, E.E. and Xu, H.: In situ AFM observations of Ca-Mg carbonate
 910 crystallization catalyzed by dissolved sulfide: Implications for sedimentary dolomite formation,
 911 *Geochemica et Cosmochemica Acta*, 105, 44-55, <https://doi.org/10.1016/j.gca.2012.11.010>, 2013b.